TU Delft

Delft University of Technology

Document Version
Final published version

Licence
CC BY-NC-ND

Citation (APA)
Xu, Z., Li, J., Zheng, Z., Huang, C., Ren, Z., Shang, G., Sun, Y., Miao, W., Zhou, N., & Zhu, Y. (2026). Dynamic feasible region characterization of tie-line transmission power for congestion management. *International Journal of Electrical Power and Energy Systems*, *181*, Article 112132. https://doi.org/10.1016/j.ijepes.2026.112132

Important note
To cite this publication, please use the final published version (if applicable).
Please check the document version above.

Copyright
In case the licence states “Dutch Copyright Act (Article 25fa)”, this publication was made available Green Open Access via the TU Delft Institutional Repository pursuant to Dutch Copyright Act (Article 25fa, the Taverne amendment). This provision does not affect copyright ownership.
Unless copyright is transferred by contract or statute, it remains with the copyright holder.

Sharing and reuse
Other than for strictly personal use, it is not permitted to download, forward or distribute the text or part of it, without the consent of the author(s) and/or copyright holder(s), unless the work is under an open content license such as Creative Commons.

Takedown policy
Please contact us and provide details if you believe this document breaches copyrights.
We will remove access to the work immediately and investigate your claim.

This work is downloaded from Delft University of Technology.

Electrical Power and Energy Systems 181 (2026) 112132



Contents lists available at ScienceDirect

International Journal of Electrical Power & Energy Systems

journal homepage: www.elsevier.com/locate/ijepes

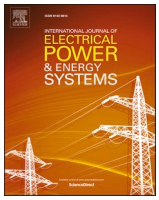

Dynamic feasible region characterization of tie-line transmission power for congestion management☆

Zhengyang Xu [a], Jie Li [a], Zixuan Zheng [a,*], Chunjun Huang [b], Zheng Ren [c], Guozheng Shang [c], Yuntao Sun [d], Weiwei Miao [d], Ning Zhou [d], Yuanzhen Zhu [d]

[a] Department of Electrical Engineering, College of Electrical Engineering, Sichuan University, Chengdu 610000, China
[b] Department of Electrical Sustainable Energy, Delft University of Technology, Delft 2600, the Netherlands
[c] State Grid Inner Mongolia Eastern Electric Power Co., Ltd., Hohhot 010000, China
[d] Electric Power Research Institute, State Grid Shandong Electric Power Co., Ltd., Jinan 250000, China

ARTICLE INFO

Keywords:
Congestion management
Dynamic feasible region
Multi-type energy storage
Line N-1 security constraints
Mixed-integer linear programming

ABSTRACT

Due to the spatial mismatch between renewable resources and demand centers in China, cross-regional renewable energy delivery is increasingly constrained by limited capacity of transmission lines, resulting in severe congestion. To exploit flexible resources while ensuring system security, this paper proposes a dynamic feasible region (DFR) characterization approach for tie-line transmission power to support congestion management. A vertex search-based model is developed to iteratively identify the boundary points of the feasible region (FR) in the tie-line transmission power space under security constraints, incorporating multi-type energy storage (ES) regulation and line N-1 security. Based on the identified DFR, an optimization model for congestion management is formulated to enhance tie-line utilization and alleviate line congestion. The obtained optimal configuration of multi-type ES is further utilized for DFR expansion, and multi-resource dispatch strategies are derived through an iterative coordination optimization framework involving repeated DFR reconstruction and congestion management optimization. Case studies conducted on a real-world system in Northern China validate the feasibility and effectiveness of the proposed approach. The results demonstrate that the approach enhances tie-line utilization, improves renewable energy accommodation, and alleviates line congestion in a cost-effective manner.

1. Introduction

1.1. Background

With the increasing penetration of renewable energy and the spatial mismatches between power generation and consumption [1], cross-regional renewable energy delivery has become a key approach for optimizing energy resource allocation. However, the limited transmission capability of lines is insufficient to meet the growing demand for high-penetration renewable energy delivery [2]. On the one hand, frequent transmission congestion is often triggered by inadequate regulation capacity and power flow security [3,4]. On the other hand, the intermittency and volatility of renewable energy during cross-regional transmission result in low tie-line utilization and severe curtailment of wind and solar power. Moreover, the simplified modeling of tie-line transmission capability fails to adequately support the improvement of tie-line utilization and reduction of line congestion risks in regional power grids [5]. Consequently, it is imperative to fully exploit the flexibility potential of regulation resources and incorporate them into the characterization of actual renewable energy delivery boundaries, so as to alleviate transmission congestion and improve renewable energy accommodation capability.

Effective congestion management necessitates the coordinated consideration of intra-regional transmission lines and cross-regional tie-lines. The existing methods concerning line congestion management mainly include network reconfiguration [6,7], flexible alternating current transmission devices [8,9], and dynamic line rating [10,11]. These methods primarily focus on congestion within regional power grids by adjusting line transmission capabilities and improving power flow distribution, thereby facilitating local renewable energy utilization. In addition, large-scale optimization allocation of electric power resources across regional power grids is achieved through cross-regional power transmission via tie-lines [12,13]. It is essential for ensuring the

☆ This work was supported by the National Natural Science Foundation of China under Grant 52277115.
* Corresponding authors.
E-mail address: scuzzx@163.com (Z. Zheng).

https://doi.org/10.1016/j.ijepes.2026.112132
Received 26 March 2026; Received in revised form 1 June 2026; Accepted 16 July 2026
Available online 21 August 2026
0142-0615/© 2026 The Authors. Published by Elsevier Ltd. This is an open access article under the CC BY-NC-ND license (http://creativecommons.org/licenses/by-nc-nd/4.0/).

Nomenclature

Abbreviations

ES	Energy storage
FR	Feasible region
DFR	Dynamic feasible region
DR	Demand response
MILP	Mixed integer linear programming
Li-B	Lithium-ion battery
CAES	Compressed air energy storage
PHS	Pumped hydro storage
SOC	State of charge

Parameters

k	Type of ES
i	Node of the regional power grid
$P_{ES,k}^{min}$, $P_{ES,k}^{max}$	Minimum and maximum rated power of ES k
$E_{ES,k}^{min}$, $E_{ES,k}^{max}$	Minimum and maximum rated capacity of ES k
$\beta_{ch,k}$, $\beta_{dis,k}$	0–1 charging and discharging state variables of ES k
$\alpha_{ch,k}$, $\alpha_{dis,k}$	Charging and discharging efficiency of ES k
$\boldsymbol{Z}$	Line state matrix
C	Set of contingency scenarios
L	Set of transmission lines
$\delta_{f(l)},\delta_{t(l)}$	Phase angles for the from-node and to-node
x_l	Reactance of line l
v	Operating state parameter of the regional power grid
P_l^{max}	Transmission limit of line l
$\boldsymbol{P}_{PG}$	Generator output matrix
$\boldsymbol{P}_{TL}$	Tie-line transmission power matrix
$\boldsymbol{P}_{Load}$	Node load matrix
$\boldsymbol{P}_L$	Line power flow matrix
$\boldsymbol{M}_{G\text{-}i}$	Generator-node incidence matrix
$\boldsymbol{M}_{l\text{-}i}$	Node-branch incidence matrix
P_L^{N-1}	Line power flow matrix in the line contingency
$P_{PG,n}^{min}$,$P_{PG,n}^{max}$	Minimum and maximum output of generator n
$\Delta P_{G,n}^{UP}$, $\Delta P_{G,n}^{DN}$	Upward and downward rate of thermal power unit n
δ_{min}, δ_{max}	Minimum and maximum limits of node phase angle
$v_{j,max}^{-}$, $v_{j,max}^{+}$	Minimum and maximum response rate of DR
T_n	The n-th time subset
E	Tolerance threshold
d_h	The normal distance
n_k	Normal vector of the k-th hyperplane
n'	Group of thermal power units in sending-end system
n''	Group of renewable energy power units in sending-end system
r	Discount rate of ES
$P_{trans'}$	Transferable load power before scheduling
P_{cut^*}	Reducible load power before reduction
θ_{rl}	Load reduction coefficient of reducible load
P_{adj}	Response power of adjustable load
$P_{NEG,n''}^{pred}$	Active dispatch output of renewable energy unit n''
$\boldsymbol{A}_{Tn}$	Coefficient matrix of the linear constraints
$\boldsymbol{b}_{Tn}$	Constant term matrix of the linear constraints
λ_{tl}	Security margin of tie-line

Decision variables

$\lambda i\ k$	0–1 configuration state variable of ES k
$P_{G,s,n'}$	Output of thermal power unit n'
$P_{NEG,n''}$	Active predicted output of renewable energy unit n''
P_{TLnl}	Transmission power of the n_l-th tie-line
P_{trans}	Transferable load power after scheduling
P_{adj}	Response power of adjustable load
P_{cut}	Reducible load power after reduction
$P_{ES,k}^{N}$	Rated power of ES k
$E_{ES,k}^{N}$	Rated capacity of ES k
$P_{ch,k}$	Charging power of ES k
$P_{dis,k}$	Discharging power of ES k

economic and secure operation of power grid dispatch to characterize tie-line transmission capability, while also providing support for line congestion management. Notably, a critical consideration in this context is that the delineation of renewable energy delivery boundaries must account for the coupling relationships among the transmission powers of different tie-lines. Moreover, temporal coupling constraints inherent in regional grid operation introduce additional complexity [14], making it challenging to characterize renewable energy transmission capability at different times. Beyond this, the regulation effects of internal resources within regional power grids can also significantly affect the transmission capability of tie-lines. Therefore, addressing the issue of imprecise characterization for tie-line transmission capability is crucial for reliable congestion management.

1.2. Literature review

In terms of characterizing the boundary of cross-regional renewable energy delivery, many studies have adopted the maximum available transfer capability method, typically evaluated based on the maximum power of boundary sections or individual tie-lines. Ref. [15] adopts the network flow method to calculate the maximum injection power at the boundary nodes of interconnected power grids. Such methods only take into account the generator capacity constraints and branch transmission limit constraints, while ignoring the power flow balance constraints in regional power grids. The maximum transfer capability of tie-line interfaces is solved through an equivalent optimal power flow model for interconnected power systems [16]. In [17], the interval total transfer capability of the grid-connected high-voltage direct current system is calculated by constructing a bi-level optimization model. There are also studies that employ the equivalent line constraint method. Ref. [18] derives the equivalent line constraints based on the consistency of available transfer capability in the external network, thereby characterizing the transmission capability of tie-lines. However, the results obtained using the aforementioned method may lack sufficient accuracy.

To characterize the actual transmission capabilities of multiple tie-lines over different times, many studies have introduced the feasible region (FR) method, which captures the coupling relationships among tie-lines by mapping their feasible transmission power into a spatial coordinate system. In [19], an improved multi-parametric programming (MPP) method is proposed to characterize the FR between two regions, and the FR boundaries are expanded through upgrading the line capacity. A unified equivalent model is constructed to precisely capture the transmission capacity region of tie-lines in [20], which fully retains the operation constraints and operation cost information of the external power grid. Ref. [21] considers the expansion effect of two flexible spaces on the FR: unit deep peak shaving and line emergency transmission rate. The FR of tie-line transmission power and the FR of power contract execution are integrated to identify the unified power trading region, which enables the joint consideration of source and sink regional networks [22]. An optimal planning model considering the identification of weak factors restricting the FR is proposed in [23], and a method is developed to strengthen these weak factors. Ref. [24] extends the two-region system to a multi-region system by analyzing the coupling relationships of security constraints between various regions. A Progressive Vertex Enumeration algorithm is proposed to efficiently solve the

equivalent projection model, which constructs the convex hull by identifying the vertices of the projection region and achieves explicit error control [25]. Ref. [26] further incorporates energy storage (ES) regulation constraints and small-signal stability constraints into the characterization. In [27], line N-1 security constraints are considered to effectively accommodate contingency scenarios. When temporal coupling constraints are taken into account, a period-by-period vertex search method combined with equivalent coupling constraints based on convex combinations is proposed to characterize the dynamic feasible region (DFR) [28]. Ref. [29] proposes a temporally coupled fast algorithm to approximate the original high-dimensional DFR by computing low-dimensional polytopes associated with different combinations. Refs. [30,31] iteratively generate feasible cutting planes via the outer progressive approximation algorithm to obtain the DFR boundaries. And in [32], a fast calculation method based on time decomposition and tie-line aggregation is proposed for FR construction in renewable energy integration scenarios. In [33], the inner-box approximation method is adopted to characterize the boundary of transmission-distribution interactive power using a box-shaped region formed by upper and lower power trajectories. Table 1 summarizes the relevant research literature on characterization methods for the FR of tie-line transmission power. Current studies mostly focus on the expansion of FR boundaries through transmission line capacity improvements or thermal power unit modifications without the consideration of other regulation resources. And the impact of line N-1 security constraints on the boundaries is not adequately incorporated into the FR characterization.

In the characterization of cross-regional renewable energy delivery boundaries employing the FR, the configuration of ES provides additional operational flexibility for congestion management and FR expansion. With the rapid advancement of ES in recent years, it has emerged as a key technology for alleviating line congestion and facilitating renewable energy accommodation, due to its superior regulation versatility, such as energy time-shifting, fast response, and flexible deployment [34,35]. Ref. [36] summarizes the relevant applications of ES in line congestion management of transmission networks. A robust optimal configuration model of ES is developed in [37], which integrates peak shaving and congestion management to improve the transmission capacity of lines via energy time-shifting. Meanwhile, the stochastic optimization model of ES based on mixed-integer linear programming (MILP) is presented in order to reduce wind power spillage and load curtailment while managing congestion and voltage deviations [38]. In [39], a short-term optimal operation model for the wind farm-pumped storage hydropower plant hybrid system is established to promote renewable energy accommodation. A strategy to improve trading efficiency by optimizing the capacity of pumped hydro storage is introduced in [40], thereby increasing power delivery reliability and improving transmission line economics. In [41], an interval-stochastic programming method is proposed for the expansion planning integrating power generation, transmission and ES to enhance the flexibility of power systems. Ref. [42] proposes a scalable optimal planning method for ES to effectively eliminate line power flow violations and enhance grid transmission margin. Ref. [43] develops an analysis framework to investigate the dynamic interplay between wind curtailment and ES, and evaluates various congestion management strategies through multiple indicators.

Hybrid ES can meet multiple demands in congestion management scenarios by integrating different ESs. Ref. [44] considers the hybrid ES comprising compressed air ES (CAES) and underground hydrogen storage, and develops a multi-period line capacity expansion planning model to enhance the transmission capability of power grid lines. In [45], an optimal scheduling strategy is proposed for hybrid ES to provide flexible dispatch power level in the wind energy generation system. An optimal scheduling method combining variational mode decomposition and MILP is proposed in [46], considering the complementary characteristics of power-based and energy-based storage methods, including the lithium-ion battery (Li-B), supercapacitor ES (SCES) and thermal storage tanks. Ref. [47] evaluates the role of pumped hydro storage (PHS) and hydrogen in enabling cost-effective power system expansion. Ref. [48] establishes a multi-objective optimal configuration model for hybrid ES, fully exploiting the advantages of hybrid ES in reducing wind and solar power curtailment and improving power quality within distributed generation systems.

1.3. Motivation

In summary, the congestion management problem of renewable-dominant cross-regional grids mentioned in this paper is described as follows. Firstly, line congestion management is limited by the imprecise modeling of tie-line transmission capabilities. Several studies [15–18] have adopted the maximum available transfer capability method and equivalent line constraint method to calculate it. The maximum available transfer capability method in existing research is typically applied to a single tie-line or corridor. However, the actual transmission capabilities are affected by coordinated limitations imposed by operation

Table 1
Comparative summary of representative characterization methods for the feasible region.

Works	FR expansion	FR considering temporal variations	Line N-1 security constraints	Method	Approximation Type
[19]	Line upgrading	×	×	MPP	/
[20]	×	×	×	MPP	/
[21]	Line upgrading /generator regulation	×	√	MPP	/
[22]	×	×	×	MPP	/
[23]	Line upgrading /generator regulation	×	×	MPP	/
[24]	×	×	×	Vertex search method	Inner approximation
[25]	×	×	×	Vertex search method	Inner approximation
[26]	Single-type ES regulation	×	×	Enumeration method	Inner approximation
[27]	×	×	√	Vertex search method	Inner approximation
[28]	×	DFR	×	Vertex search method	Inner approximation
[29]	×	DFR	×	Vertex search method	Inner approximation
[30]	×	DFR	×	Outer progressive approximation	Outer approximation
[31]	×	DFR	×	Outer progressive approximation	Outer approximation
[32]	×	DFR	×	Vertex search method	Inner approximation
[33]	×	DFR	×	Box-shaped inner approximation	Inner approximation
Proposed	Multi-type ES regulation	DFR	√	Vertex search method	Inner approximation

constraints within the regional power grid across multiple tie-lines or corridors, making results based on it potentially imprecise. And the equivalent line constraint method only calculates specific power combinations at the boundary section within a single time interval, which does not take all relevant constraints into account. Additionally, several studies have adopted FR to characterize the actual transmission capability of different tie-lines, as summarized in Table 1. However, some studies fail to consider the dynamic interdependence among multiple periods and only depict static FRs at individual time points, thereby causing the FR boundaries to deviate from the actual transmission capability. Meanwhile, with the continuous development of flexible resources, their regulation effects on the FR boundaries have not been adequately incorporated, resulting in FR boundaries being constrained by the limited regulation capabilities of conventional power supplies. Moreover, most existing studies focus on tie-line power exchange in the base operating scenario, while ignoring the impact of power flow variations caused by N-1 contingencies on the FR. Without the correction provided by these security constraints, the FR boundaries will lead to an overestimation of the tie-line transmission capability. In addition, the regulation potential of flexible resources for the sending-end region in these studies has not been fully leveraged. Although several studies have investigated congestion management through the participation of ES, most studies focus on the given types of single or hybrid ES, while rarely incorporating ES selection into the optimization framework. As a result, the regulation capability of ES is constrained by pre-defined modeling parameters which fail to capture the heterogeneous regulation characteristics and complementary capabilities among diverse ESs. Furthermore, existing research methods primarily focus on congestion management of intra-regional transmission lines, while neglecting the coordinated congestion management between intra-regional transmission lines and cross-regional tie-lines. Consequently, the large-scale optimal allocation of electric power resources across regional power grids is difficult to achieve. Therefore, there is an urgent need to fully exploit the flexibility potential of regulation resources and incorporate it into the FR characterization to support congestion management.

Aiming at addressing the existing research gap, the key novelty of this paper is: the characterization for the DFR of tie-line transmission power, which enables a precise representation of the real-time cross-regional renewable energy delivery boundary for congestion management. In particular, the regulation capabilities of multi-type ES and line N-1 security constraints are explicitly incorporated into the characterization for the DFR. On this basis, the optimization model for line congestion management is developed to promote renewable energy accommodation and alleviate line congestion.

1.4. Contributions

The main contributions of this paper can be summarized as follows:

(a) A DFR characterization framework based on the vertex search method and time decomposition strategy is developed to describe the boundaries of cross-regional renewable energy delivery for congestion management, incorporating the regulation capability of multi-type ES and line N-1 security constraints.
(b) An MILP-based line congestion management optimization model is constructed. The optimal configuration of multi-type ES is obtained for FR expansion, and the multi-resource regulation strategy is further determined through iterative coordination optimization to alleviate line congestion.
(c) The feasibility of the proposed DFR characterization approach supporting congestion management is validated based on a real-world renewable-dominant cross-regional delivery system in North China and the IEEE 30-IEEE 39 test system.

The remainder of this paper is organized as follows. In Section II, a vertex search method-based boundary search model for the FR of tie-line transmission power is proposed. Section III establishes an optimization model for line congestion management of renewable-dominant cross-regional grids within the framework of the FR. Section IV presents results and discussion based on case studies. Conclusions and future work are drawn in Section V.

2. Dynamic feasible region characterization approach

2.1. Multi-dimensional security constraint set

It is essential for line congestion management to explicitly identify the boundary of cross-regional renewable energy delivery through characterizing the DFR, which incorporates the multi-dimensional security constraints of regional power grids. As indicated in Ref. [49], these security constraints can be mathematically represented as a convex polytope in a high-dimensional space. Accordingly, by projecting this polytope onto the tie-line transmission power space, a visual analysis framework based on security constraints projection is established to characterize the DFR of tie-line transmission power. Specifically, it mainly includes the constraints on regulation capability of ES, line N-1 security constraints and fundamental multi-dimensional security constraints. The latter comprises the limits of line power flow, node phase angle, outputs of renewable energy and thermal power units, coupled with power balance and demand response (DR) regulation constraints. Meanwhile, temporal coupling constraints of thermal power units, DR and ES are also explicitly considered. In addition, the FR of tie-line transmission power exhibits dynamic temporal evolution, driven by the time-varying nature of generator outputs, nodal loads and power flow distributions, which uniquely reshape the boundaries at different times. Moreover, under a scheduling horizon of T and with N tie-lines, the DFR characterization is transformed into a high-dimensional hyperplane solving problem in an $N \times T$ dimensional space. The schematic of high-dimensional polytope projection onto the tie-line transmission power space is shown in Fig. 1.

For the constraints on regulation capability of ES, decision variables representing configuration types are introduced to couple the differentiated regulation boundaries of multi-type ES, which can be expressed as:

$$\boldsymbol{\lambda} = \begin{bmatrix} \lambda_1^1 & \lambda_1^2 & \cdots & \lambda_1^i \\ \vdots & \vdots & \cdots & \vdots \\ \lambda_k^1 & \lambda_k^2 & \cdots & \lambda_k^i \\ \vdots & \vdots & \vdots & \vdots \\ \lambda_K^1 & \lambda_K^2 & \cdots & \lambda_K^i \end{bmatrix} \tag{1}$$

where k denotes the ES type; i represents the node of the regional power grid; λ_k^i is a 0–1 variable, indicating the configuration state of ES k at node i; K is the number of ES types.

In the constraints on rated power and capacity of multi-type ES, the

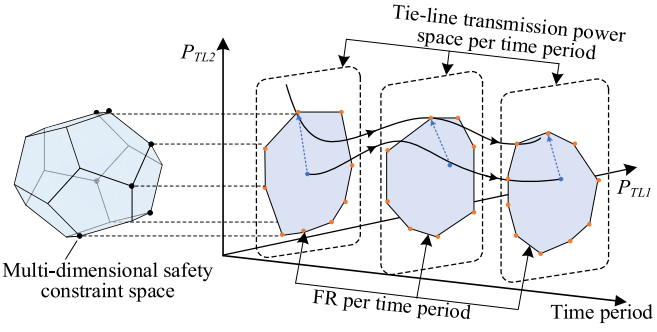

Fig. 1. Schematic of high-dimensional polytope projection.

nonlinearity caused by the multiplication of 0–1 and continuous variables is addressed using the Big-M method to linearize the constraints, which are as follows:

$$\begin{cases} 0 \leqslant \sum_{n=1}^{k} \lambda_n^i \leqslant 1, \ \forall i \\ \lambda_k^i P_{ES,k}^{\min} \leqslant P_{ES,k}^N \leqslant \lambda_k^i P_{ES,k}^{\max} \\ \lambda_k^i E_{ES,k}^{\min} \leqslant E_{ES,k}^N \leqslant \lambda_k^i E_{ES,k}^{\max} \end{cases} \tag{2}$$

where $P_{ES,k}^N$ denotes the rated power of ES k; $P_{ES,k}^{min}$ and $P_{ES,k}^{max}$ represent the minimum and maximum values of the configuration rated power for ES k; $E_{ES,k}^N$ is the configuration capacity of ES k; $E_{ES,k}^{min}$ and $E_{ES,k}^{max}$ indicate the minimum and maximum values of the configuration capacity for ES k.

Multi-type ES can be charged and discharged continuously within rated power ranges. Their charging and discharging states can be represented by 0–1 variables $\beta_{ch,k}(t)$ and $\beta_{dis,k}(t)$. The operating power constraints are linearized using the Big-M method, which can be expressed as:

$$\begin{cases} 0 \leqslant P_{ch,k}(t) \leqslant \beta_{ch,k}(t) P_{ES,k}^N \\ 0 \leqslant P_{dis,k}(t) \leqslant \beta_{dis,k}(t) P_{ES,k}^N \\ \beta_{ch,k}(t) + \beta_{ch,k}(t) \leqslant 1 \end{cases} \tag{3}$$

where $P_{ch,k}(t)$ and $P_{dis,k}(t)$ are the charging and discharging power of ES k at time t; $\beta_{ch,k}(t)$ and $\beta_{dis,k}(t)$ represent the charging and discharging states of ES k at time t.

In addition, multi-type ES is constrained by the state of charge (SOC), which are as follows:

$$\begin{cases} 0 \leqslant soc_k(t) \leqslant 100\% \\ soc_k(t+1) = soc_k(t) + \dfrac{(P_{ch,k}(t)\alpha_{ch,k} + P_{dis,k}(t)/\alpha_{dis,k})}{E_{ES,k}^N} \\ soc_k^0 = soc_k^{end} \end{cases} \tag{4}$$

where soc_k^0, $soc_k(t)$ and soc_k^{end} represent the SOC of ES k at the initial time, time t and end time; $\alpha_{ch,k}$ and $\alpha_{dis,k}$ are the charging and discharging efficiencies of ES k.

For the line N-1 security constraints, the power system is required to remain secure and stable in the event of a single line contingency [50]. The operating state of the line can be represented as:

$$\boldsymbol{Z} = \begin{bmatrix} Z_1^1 & Z_1^2 & \cdots & Z_1^L \\ Z_2^1 & Z_2^2 & \cdots & Z_2^L \\ \vdots & \vdots & & \\ Z_C^1 & Z_C^2 & \cdots & Z_C^L \end{bmatrix} \tag{5}$$

where $\boldsymbol{Z}$ is the line state matrix; Z_c^l denotes the operating state of line l in contingency scenario c; C and L represent the number of contingency scenarios and the number of transmission lines in the regional power grid.

In this paper, a direct current power flow model is adopted to formulate the linearized line flow constraints [51]:

$$P_l(t) = \frac{\delta_{f(l)}(t) - \delta_{t(l)}(t)}{x_l} \cdot (\upsilon + Z_c^l - \upsilon \cdot Z_c^l) \tag{6}$$

where $P_l(t)$ denotes the power flow of line l at time t; $\delta_{f(l)}(t)$ and $\delta_{t(l)}(t)$ are the phase angles at the from-node and to-node of line l at time t; x_l represents the reactance of line l; υ signifies the operating state parameter of the regional power grid; $\upsilon = 1$ indicates that the regional power grid is in normal operation, and $\upsilon = 0$ indicates that the regional power grid malfunctions.

The power balance constraint and line transmission limits can be expressed as:

$$\begin{cases} -P_l^{\max} \leqslant P_l(t) \leqslant P_l^{\max} \\ \boldsymbol{M}_{G-i}\boldsymbol{P}_G(t) - \boldsymbol{P}_{TL}(t) = \boldsymbol{P}_{Load}(t) + \boldsymbol{M}_{L-i}(\upsilon \boldsymbol{P}_L(t) + (1-\upsilon)\boldsymbol{P}_L^{N-1}(t)) \end{cases} \tag{7}$$

where P_l^{max} denotes the transmission limit of line l in the regional power grid; $\boldsymbol{P}_{PG}(t)$, $\boldsymbol{P}_{TL}(t)$, $\boldsymbol{P}_{Load}(t)$ and $\boldsymbol{P}_L(t)$ represent the generator output matrix, tie-line transmission power matrix, node load matrix, and line power flow matrix at time t; $\boldsymbol{M}_{G\text{-}i}$ and $\boldsymbol{M}_{l\text{-}i}$ are the generator-node incidence matrix and node-branch incidence matrix; $\boldsymbol{P}_L^{N-1}(t)$ indicates the line power flow matrix at time t in the N-1 line contingency scenario.

Renewable energy and thermal power units are constrained by their output limits, which can be expressed as:

$$P_{PG,n}^{min} \leqslant P_{PG,n}(t) \leqslant P_{PG,n}^{max} \tag{8}$$

where $P_{PG,n}^{min}$ and $P_{PG,n}^{max}$ are the minimum and maximum output of generator n; $P_{PG,n}(t)$ denotes the output of generator n at time t.

Thermal power units should also satisfy temporal coupling constraints:

$$\begin{cases} P_{G,n}(t) - P_{G,n}(t-1) \leqslant \Delta P_{G,n}^{UP} \\ P_{G,n}(t+1) - P_{G,n}(t) \leqslant \Delta P_{G,n}^{DN} \end{cases} \tag{9}$$

where $\Delta P_{G,n}^{UP}$ and $\Delta P_{G,n}^{DN}$ denote the upward and downward rate of thermal power unit n.

The phase angles of nodes are constrained by upper and lower bounds, which can be expressed as

$$\delta_{min} \leqslant \delta_i(t) \leqslant \delta_{max} \tag{10}$$

where $\delta_i(t)$ denotes the phase angle of node i at time t; δ_{max} and δ_{min} represent the upper and lower limits of node phase angle variation.

The DR is constrained by response power and response rate, which are as follows:

$$\begin{cases} P_{i,\min}(t) \leqslant P_{var}(t) \leqslant P_{i,\max}(t) \\ v_{j,\max}^- \leqslant P_{var}(t) - P_{var}(t-1) \leqslant v_{j,\max}^+ \end{cases} \tag{11}$$

where $P_{i,\max}(t)$ and $P_{i,\min}(t)$ are the maximum and minimum response power of DR at time t; $P_{\text{var}}(t)$ denotes the response power of DR at time t; $v_{j,max}^+$ and $v_{j,max}^-$ represent the upward and downward ramping rates of DR loads.

2.2. Analysis of the DFR characterization

Based on the analysis in Section II (A), the fundamental multi-dimensional security constraint set of the regional power grid can be expressed as:

$$G(P_{TL}, y, z) \leqslant 0 \tag{12}$$

where P_{TL} signifies a projection variable representing the physical quantity corresponding to the feasible solution after projection; y is the regulation variable which can change the position of the feasible solution in the FR, including the dispatch output of renewable energy units and thermal power units, flexible loads, etc.; z represents the constant quantity.

The FRs of tie-line transmission power at different times are characterized by considering the fundamental multi-dimensional security constraints, incorporating the regulation capability of multi-type ES and line N-1 security constraints. The structure of the proposed characterization approach is shown in Fig. 2.

The fundamental multi-dimensional security space of the regional power grid can be projected onto the lower-dimensional space corresponding to tie-line transmission power, which is as follows:

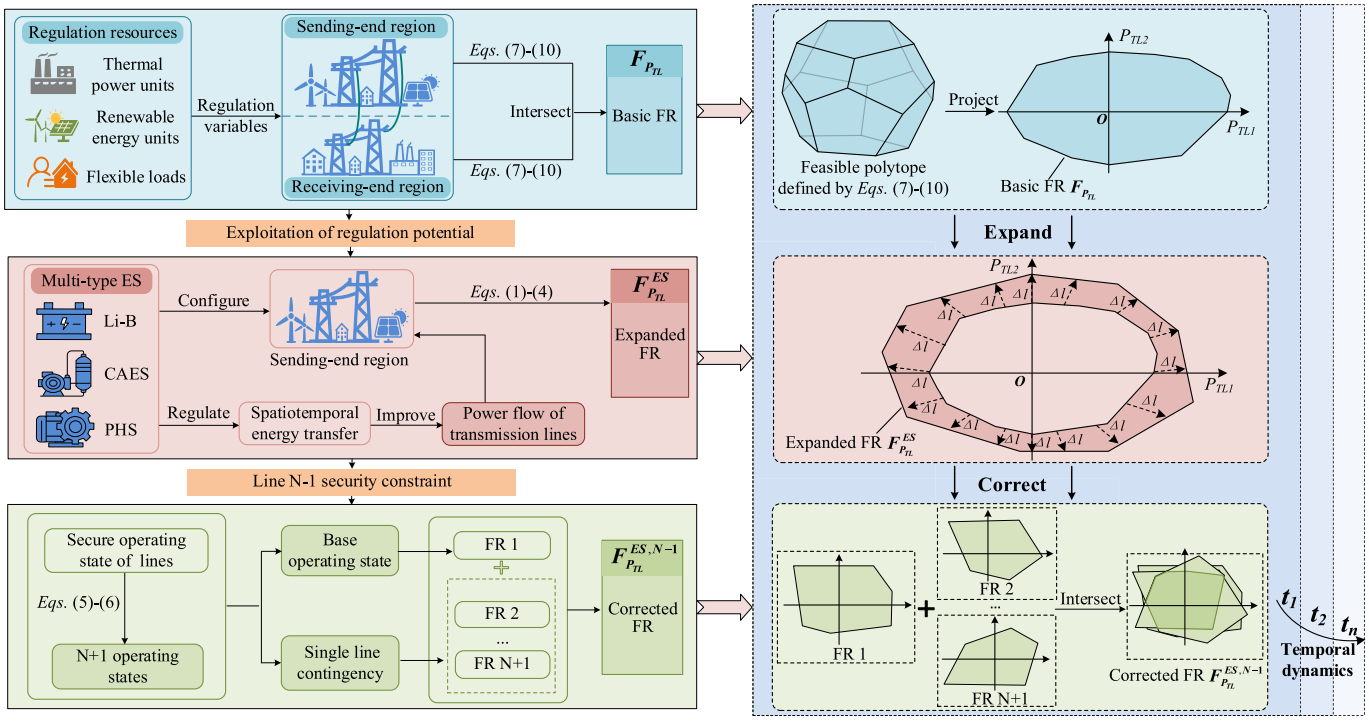

Fig. 2. Schematic of DFR characterization approach.

$$F_{P_{TL}} = \{P_{TL} \in R^{N_{TL}\times T} | \exists y,\ s.t.\ G(P_{TL}, y, z) \leqslant 0\} \tag{13}$$

where F_{PTL} denotes the fundamental FR without considering the regulating capacity of multi-type ES and the line N-1 security constraints.

Multi-type ES is regarded as a valuable regulation resource within regional power grids, enabling spatiotemporal shifting of electric energy with its flexible regulation capabilities. By incorporating it into the regional power grid operation model as a regulation variable, the fundamental FR F_{PTL} limited by the regulation capabilities of conventional power supplies and grid security constraints can be substantially expanded. Accordingly, the adjustable range of tie-line transmission power and potential for optimal resource allocation are improved. The FR of tie-line transmission power can be uplifted to a higher-dimensional FR $F_{PES,\ PTL}$ with the ES operating power and tie-line transmission power as independent variables considering regulation capabilities of multi-type ES, which can be expressed as:

$$F_{P_{ES},P_{TL}} = \{(P_{ES}, P_{TL})\} \in R^{(N_{ES}+N_{TL})\times T} \tag{14}$$

where N_{ES} and N_{TL} denote the number of multi-type ES and tie-lines; T represents the regulated cycle.

Taking the tie-line transmission power as the analysis object, the FR $F_{PES,\ PTL}$ is projected onto the tie-line transmission power space to characterize the FR of tie-line transmission power incorporating the regulation capabilities of multi-type ES, which can be expressed as follows:

$$F_{P_{TL}}^{ES} = \{P_{TL} \in R^{N_{TL}\times T} | \exists P_{ES}, s.t.(P_{ES}, P_{TL}) \in F_{P_{ES},P_{TL}}\} \tag{15}$$

where $F_{PTL}^{ES,N-1}$ denotes the expanded FR of tie-line transmission power considering the regulation capabilities of multi-type ES.

Multi-type ES enables the FR to gain expansion space by improving line power flows. The boundaries of FR are significantly affected by line contingencies, making it necessary to consider the line N-1 security constraints for system operation. By coupling the security constraints of the base-state operating scenario with single-line contingency scenarios at a certain time point, the final FR is corrected by intersecting the FRs of all considered scenarios, which can be calculated by:

$$F_{P_{TL}}^{ES,N-1} = F_{P_{TL},0}^{ES} \cap F_{P_{TL},k=1}^{ES} \cap \ldots \cap F_{P_{TL},k=l}^{ES} \cap \ldots \cap F_{P_{TL},k=N_l}^{ES} \tag{16}$$

where $F_{PTL}^{ES,N-1}$ is the corrected FR; $F_{PTL,0}^{ES}$ represents the FR of the base-state operating scenario; $F_{PTL,k=1}^{ES}$ indicates the FR of line l contingency scenario; N_l signifies the number of lines.

Accordingly, the FR of tie-line transmission power for the regional power grid considering the security operation constraint set can be expressed as:

$$\begin{cases} F_{P_{TL}}^{ES,N-1} = \{F_{send}, F_{recv}\} \\ Y = \{Y_{send}, Y_{recv}\} \\ G = \{G_{send}, G_{recv}\} \end{cases} \tag{17}$$

where F_{send} and F_{recv} are the export FR and injection FR of the sending-end and receiving-end regional power grids; Y_{send} and Y_{recv} denote the regulation variables of the sending-end and receiving-end regional power grids; G_{send} and G_{recv} represent the security constraint sets of the sending-end and receiving-end regional power grids.

The resulting FR of tie-line transmission power is given by the intersection of the FRs corresponding to the sending-end and receiving-end regional power grids, which can be calculated by:

$$F_{end} = F_{send} \cap F_{recv} \tag{18}$$

The FR represents the actual transmission capability of tie-lines, reflecting the power export capability of the sending-end region in conjunction with the power acceptance capability of the receiving-end region.

In summary, the original fundamental FR boundaries of tie-line transmission power are modified by considering the regulation capabilities of multi-type ES and line N-1 security constraints. The physical significance is represented by the dynamic adjustment for the transmission capabilities of tie-lines and intra-regional lines incorporating the regulation of ES, which optimizes the utilization boundaries of line transmission potential. Furthermore, incorporating N-1 security constraints proactively alleviates congestion risks arising from line

contingencies, thus enabling effective congestion management for renewable-dominant cross-regional grids.

2.3. Boundary characterization of the FR based on the vertex search method

Based on the theoretical derivations and analyses in Section II (A) and Section II (B), the boundary of the DFR is defined as a polytope enclosed by all hyperplanes corresponding to critical operating conditions in an $N \times T$ dimensional space. A vertex search based method [25] is adopted to characterize the DFR boundary. The method iteratively searches along outward normal directions to identify new extreme vertices and continuously updates the convex hull with the newly obtained boundary vertices, thereby progressively approximating the complete boundary of the DFR. And, due to the temporal coupling constraints, the tie-line transmission power $P_{TL1}(t)$, $P_{TL2}(t)$, …, $P_{TLN}(t)$ at time t is intrinsically coupled with those at other times. Accordingly, the DFR is represented in a high-dimensional space defined as $\Omega_{N,T} = (P_{TL1}(1), P_{TL2}(1), P_{TL1}(2), P_{TL2}(2), \ldots, P_{TL1}(T), P_{TL2}(T))$. When $N \times T$ becomes large, constructing the DFR using a vertex search method requires massive iterative updates of high-dimensional vertices, leading to an extremely heavy computational burden. Therefore, the proposed approach decomposes the DFR characterization problem over T consecutive time periods into T_n lower-dimensional continuous-time optimization subproblems, each involving a subset of m time periods. By characterizing the DFR for each subset, the original high-dimensional DFR could be approximately represented, thereby significantly reducing the computational burden. For each time subset, the DFR is obtained adopting the vertex search method. The detailed algorithm is as follows:

For any given search direction vector $\boldsymbol{\alpha}$, the following optimization model is formulated:

$$\begin{cases} \max \boldsymbol{\alpha}^T \boldsymbol{P}_{TL,T_n} \\ \boldsymbol{P}_{TL,T_n} = [P_{TL1,T_n^1}, \ldots P_{TLN,T_n^1}, P_{TL1,T_n^2}, \ldots P_{TLN,T_n^2}, \ldots, P_{TL1,T_n^m}, \ldots P_{TLN,T_n^m}] \\ s.t.\ G(P_{TL}, y, z) \leqslant 0, G_{ES}(P_{ES}, E_{ES}, SOC) \leqslant 0 \end{cases} \tag{19}$$

where $\boldsymbol{P}_{TL,Tn}$ is the tie-line transmission power matrix corresponding to the time subset T_n; $G_{ES}(\cdot)$ denotes the multi-type ES constraints.

Firstly, extreme-value searches are performed along predefined directions in each dimension to construct an initial convex hull, which can be expressed as:

$$\mathscr{K}^{(0)} = \mathrm{Conv}(V^{(0)}) \tag{20}$$

The convex hull boundary in the high-dimensional space consists of multiple hyperplanes. Defining $[v_1, v_2, \ldots, v_d]$ as the vertices of the k-th hyperplane within the current convex hull, the boundary is iteratively refined along the outward normal direction of the hyperplane, which can be calculated as:

$$\begin{cases} \max \boldsymbol{n}_{k,n}^T \boldsymbol{P}_{TL,T_n} \\ \boldsymbol{U}_k^T \boldsymbol{n}_k = 0 \\ \boldsymbol{U}_k = [v_2 - v_1, v_3 - v_1, \ldots v_d - v_1] \\ \boldsymbol{n}_{k,n} = \boldsymbol{n}_k / \|\boldsymbol{n}_k\| \end{cases} \tag{21}$$

where $\boldsymbol{U}_k$ denotes the matrix composed of a set of linearly independent tangent vectors within the k-th hyperplane, which is used to determine the normal vector of the hyperplane; $\boldsymbol{n}_k$ denotes the normal vector of the k-th hyperplane; and $\boldsymbol{n}_{k,n}$ denotes the unit normal vector of the k-th hyperplane.

If the distance between the newly identified boundary point and the current hyperplane exceeds the prescribed tolerance threshold, the new vertex is incorporated into the boundary vertex set and the convex hull is subsequently updated as follows:

$$\begin{cases} d_h = \boldsymbol{n}_{k,n}^T \boldsymbol{P}_{TL,T_n} - b_k \\ V^{(k+1)} = \begin{cases} V^{(k)} \cup \{p_{new}\}, & d_h > \varepsilon \\ V^{(k)}, & d_h \leqslant \varepsilon \end{cases} \end{cases} \tag{22}$$

where d_h denotes the normal distance between the newly identified boundary point and the current hyperplane; b_k denotes the distance from the k-th hyperplane to the origin; ε represents the tolerance threshold used to control the boundary approximation accuracy. $\{p_{new}\}$ is the set of newly generated boundary points in the current iteration.

During the iterative process, the iteration terminates once all boundary hyperplanes satisfy $d_h \leq \varepsilon$, thereby yielding the final convex FR boundary. The flowchart of DFR characterization based on the vertex search method in Eqs. (19)-(22) is shown in Fig. 3. For each single-line contingency, the boundary point pairs obtained by solving the model are recorded to construct the DFR boundary corresponding to that contingency scenario. The DFR boundaries of all contingency scenarios are then intersected to determine the final DFR space.

3. Optimization model for transmission line congestion management

This section elaborates on the optimization framework for congestion management of renewable-dominant cross-regional grids, and elucidates the iterative coordination optimization mechanism between this framework and the DFR characterization. Furthermore, the multi-objective functions of the proposed approach are transformed into a comprehensive benefits function by quantifying the wind and solar curtailment penalty cost, tie-line delivery power revenue, ES configuration cost and multi-resource regulation cost. Additionally, equations and inequalities representing constraints are established, encompassing thermal power units, DR, multi-type ES, and tie-line.

3.1. Framework for congestion management

Building upon the DFR characterization approach in Section II, this study concentrates on an optimal congestion management strategy for renewable-dominant cross-regional grids based on the DFR of tie-line transmission power. The structure of the proposed strategy is shown in Fig. 4.

(1) The initial step involves characterizing the DFR of tie-line transmission power, which serves as the real-time boundary for cross-regional renewable energy delivery within the framework of congestion management. The actual transmission capability of tie-lines is jointly constrained by the security operation conditions of the sending-end and receiving-end regions. Based on the vertex search method, the security operation high-dimensional polytopes of two regions are projected onto the tie-line transmission power space, which are intersected to characterize the DFR. In this step, the regulation capability of ES and line N-1 security constraints are considered when characterizing the DFR boundary, while the configuration scheme of multi-type ES is provided by the solution of the congestion management optimization model. Further details of this step can be found in Section II.

(2) The second step focuses on establishing the optimization model for congestion management of renewable-dominant cross-regional grids. In this process, the DFR is applied as the boundary for tie-line transmission power. 0–1 variables are introduced to represent the configuration types of ES, thereby coupling their heterogeneous regulation capability. Meanwhile, the regulation characteristics of thermal power units, DR resources, and other resources involved in congestion management are explicitly modeled. Furthermore, the optimization model is constructed by

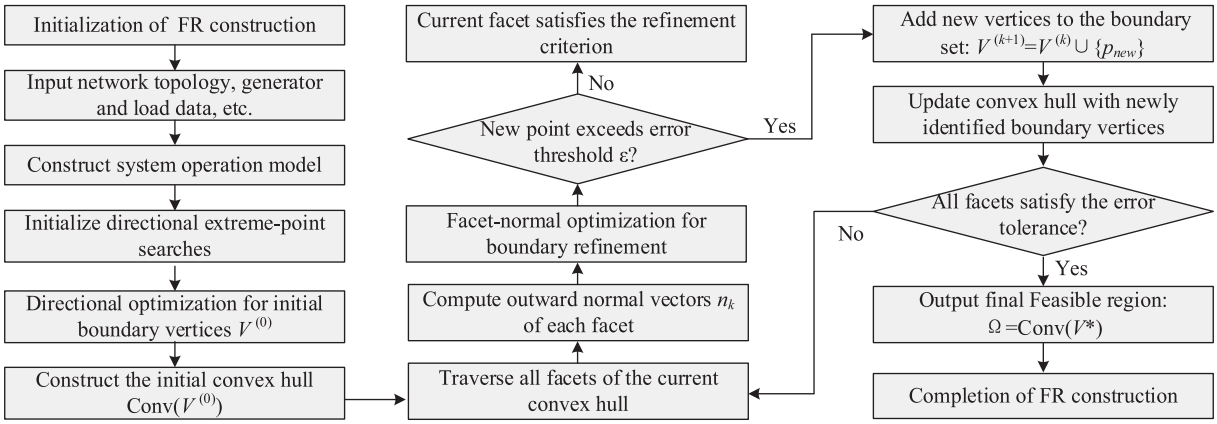

Fig. 3. Flowchart of DFR characterization based on the vertex search method.

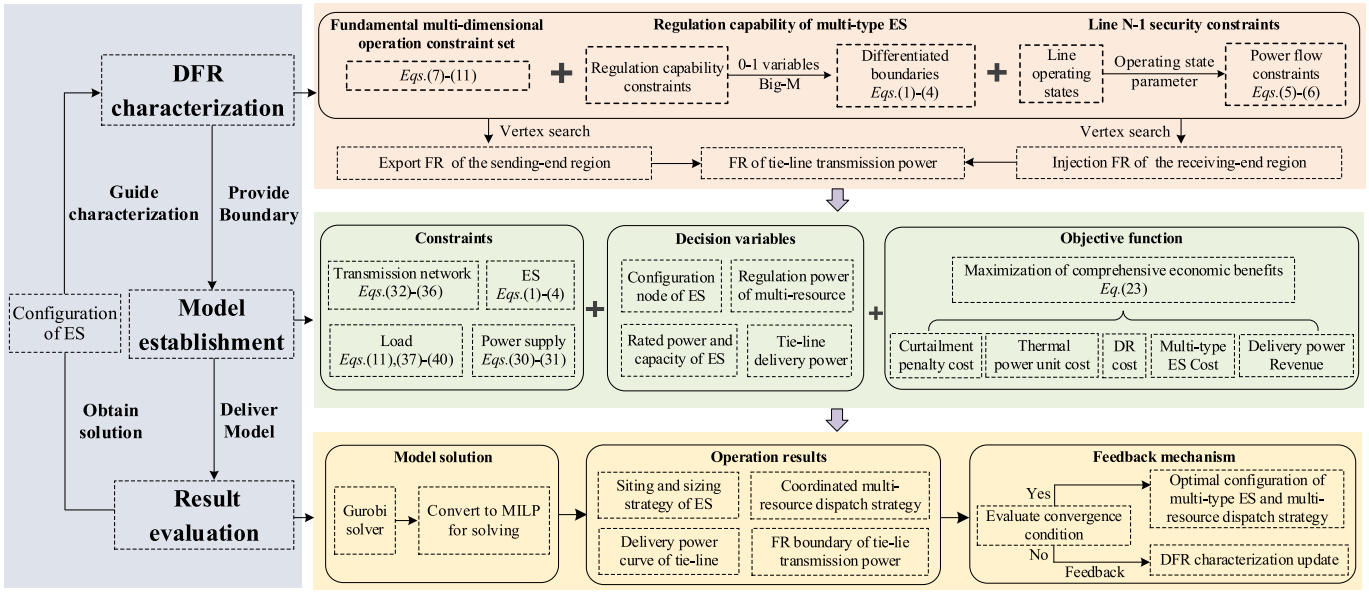

Fig. 4. Diagram of the MILP-based congestion management strategy.

incorporating performance indicators including the renewable energy accommodation rate and delivery power into the objective function as economic metrics in conjunction with system regulation costs. This detailed process is discussed further in Section III (B).

(3) In the third step, a model-solving and result-feedback process is established. The congestion management optimization model is solved through an MILP approach, and the resulting multi-type ES configuration scheme is fed back to the DFR characterization model. During the iterative coordination optimization process, convergence is achieved when the variations in ES configuration and economic objective gradually diminish and eventually stabilize, leading to a final solution. Accordingly, the optimal configuration of multi-type ES and coordinated multi-resource dispatch strategy are derived to effectively achieve power balance and congestion management. This process is detailed in Section III and Section II (B).

3.2. Optimization strategy for congestion management based on MILP

3.2.1. Objective function

Considering various costs and revenues in the system during the optimal configuration, a linear weighting is applied to formulate an objective function that maximizes the overall economic benefits of the system, which is calculated as follows:

$$\max E = \lambda_1 R_{P_{TL}} - \lambda_2 C_{Gen} - \lambda_3 C_{ES} - \lambda_4 C_{DR} - \lambda_5 C_{cur} \tag{23}$$

where E denotes the comprehensive economic benefits of the system; R_{PTL} represents the revenue from tie-line transmission power; C_{Gen} represents the thermal power units operating cost; C_{ES} indicates the multi-type ES cost; C_{DR} is the DR cost; C_{cur} denotes the wind and solar curtailment penalty cost; λ_1, λ_2, λ_3, λ_4, λ_5 signify the weight coefficients corresponding to each type of economic indicator.

3.2.1.1. Sub-objective on tie-line delivery power revenue. The revenue obtained from tie-line power export can be expressed as:

$$R_{P_{TL}} = \sum_{t}^{T} \sum_{l}^{N_l} P_{TL,l}(t) \times b_{TL} \tag{24}$$

where $P_{TL,l}(t)$ denotes the transmission power of the tie-line l at time t; N_l represents the number of tie-lines; b_{TL} indicates the unit revenue from delivery power.

3.2.1.2. Sub-objective on thermal power units operating cost. Thermal

power units involve generation costs, while a carbon emission penalty factor is applied to support the decarbonization targets, which can be calculated as:

$$C_{Gen} = \sum_{t}^{T} \sum_{n'}^{N'} \left(\left(c_{P_1,n'} + c_{P_2,n'} \right) \times P^{t}_{G,s,n'} \right) \tag{25}$$

where n' denotes the group of thermal power units in the sending-end region; $c_{P1,n'}$ represents the power generation cost of thermal power units; $c_{P2,n'}$ indicates the carbon emissions social cost of thermal power units; $P_{G,s,n'}$ (t) signifies the output of thermal power unit n' in the sending-end region at time t.

3.2.1.3. Sub-objective on multi-type ES cost. The multi-type ES cost is determined by integrating the investment cost for configuration with the associated operation and maintenance cost, which can be expressed as:

$$\begin{cases} C_{ES} = \sum_{k=1}^{K} (C^{day}_{inv,k} + C^{day}_{op,k}) \\ C^{day}_{inv,k} = \dfrac{R_{ES,k}}{365} (c_{inv,E,k} S^{N}_{ES,k} + c_{inv,P,k} P^{N}_{ES,k}) \\ C^{day}_{op,k} = \dfrac{R_{ES,k}}{365} \sum_{t}^{T} c_{op,k} \left| P_{ES,k}(t) \right| \\ R_{ES,k} = \dfrac{r(1+r)^{T_{ES,k}}}{(1+r)^{T_{ES,k}} - 1} \end{cases} \tag{26}$$

where k denotes the type of ES; $C^{day}_{inv,k}$ and $C^{day}_{op,k}$ represent the daily construction cost and operation and maintenance cost of ES k amortized to a typical day; $R_{ES,k}$ indicates the conversion coefficient of ES k; $c_{inv,E,k}$ and $c_{op,P,k}$ are the unit capacity investment cost, unit power investment cost, and unit power operation and maintenance cost of ES k over its service life; $S^{N}_{ES,k}$ signifies the configured capacity of ES k; $T_{ES,k}$ denotes the service life of ES k; r is the discount rate; $P_{ES,k}(t)$ is the charging and discharging power of ES k at time t.

In particular, the frequent charging and discharging behavior of Li-B leads to capacity degradation. Therefore, the degradation cost is quantitatively evaluated based on the depth of discharge (DOD) through experimental data fitting, so as to more accurately reflect the cost of ES, which can be calculated as:

$$\begin{cases} H_{DOD}(t) = \dfrac{E_t - E_{t-1}}{E^{N}_{ES,k}} \\ N_{cyc}(t) = N_{full} (H_{DOD}(t))^{-d} \\ C^{day}_{inv,Li-B} = \sum_{t}^{T} \dfrac{c_{inv,E,Li-B} S^{N}_{ES,Li-B} + c_{inv,P,Li-B} P^{N}_{ES,Li-B}}{N_{cyc}(t)} \end{cases} \tag{27}$$

where $H_{DOD}(t)$ denotes the DOD of ES during a single charging/discharging process at time t; E_t represents the real-time stored energy of ES at time t, $N_{cyc}(t)$ denotes the maximum charging/discharging cycle number of ES at time t when the DOD is $H_{DOD}(t)$; N_{full} represents the maximum charging/discharging cycle number when the DOD equals 1; and d is the fitting parameter, with $d = 1.5$; $c_{inv,E,Li\text{-}B}$ and $c_{inv,P,Li\text{-}B}$ denote the unit investment costs of power and capacity of the Li-B; $S^{N}_{ES,Li-B}$ and $P^{N}_{ES,Li-B}$ represent the configuration rated power and rated capacity of the Li-B.

3.2.1.4. Sub-objective on DR cost. User comfort and the overall electricity consumption quality may be compromised by the participation of flexible loads in DR. Therefore, appropriate compensation must be provided to users and is expressed as:

$$\begin{cases} C_{DR} = C_{adj} + C_{cut} + C_{trans} \\ C_{adj} = \sum_{t=1}^{T} K_{adj} \left| P_{adj}(t) \right| \\ C_{trans} = \sum_{t=1}^{T} K_{trans} \left| P_{trans'}(t) - P_{trans}(t) \right| \\ C_{cut} = \sum_{t=1}^{T} K_{cut} (P_{cut*}(t) - P_{cut}(t)) \end{cases} \tag{28}$$

where C_{adj} is the total adjustment cost of adjustable load; C_{cut} denotes the total reduction cost of reducible load; C_{trans} represents the total transfer cost of transferable load; $P_{adj}(t)$ indicates the response power of adjustable load at time t; K_{adj} signifies the compensation price per unit power of load adjustment; K_{trans} is the compensation price per unit power of load transfer; $P_{trans'}(t)$ and $P_{trans}(t)$ denote the transferable load power at time t before and after scheduling; T represents the scheduling cycle; $P_{cut*}(t)$ and $P_{cut}(t)$ indicate the load power at time t before and after reduction; K_{cut} signifies the compensation price per unit power of load reduction.

3.2.1.5. Sub-objective on wind and solar curtailment cost. The effectiveness of congestion management is reflected by the renewable energy accommodation rate. Accordingly, renewable energy curtailment is quantified as a penalty cost, which can be expressed as:

$$\begin{cases} P_{cur} = \sum_{t=1}^{T} \sum_{n=1}^{N} (P^{pred}_{NEG,n''}(t) - P_{NEG,n''}(t)) \\ C_{cur} = P_{cur} c_{cur} \end{cases} \tag{29}$$

where N denotes the number of renewable energy units; n'' signifies the group of renewable energy units in the sending-end region; $P^{pred}_{NEG,n''}$ (t) and $P_{NEG,n''}(t)$ are the active dispatch output and active predicted output of renewable energy unit n'' at time t; P_{cur} is the total wind and solar curtailment; c_{cur} is the penalty cost per unit wind and solar curtailment.

3.2.2. Constraints

In the optimization model for transmission line congestion management of renewable-dominant cross-regional grids, four primary categories of constraints are primarily incorporated.

3.2.2.1. Constraints on the power supply. The thermal power units can be regulated continuously by power range and ramp rate, which are expressed as follows:

$$\begin{cases} P^{\min}_{G,s,n'} \leqslant P_{G,s,n'}(t) \leqslant p^{\max}_{G,s,n'} \\ P_{G,s,n'}(t) - P_{G,s,n'}(t-1) \leqslant \Delta^{up}_{G,s,n'} \\ P_{G,s,n'}(t-1) - P_{G,s,n'}(t) \leqslant \Delta^{down}_{G,s,n'} \end{cases} \tag{30}$$

where $P^{max}_{G,s,n'}$ and $P^{min}_{G,s,n'}$ are the maximum and minimum technical output of thermal power unit n' in the sending-end region; $P_{G,s,n'}(t)$ represents the output of thermal power unit n' in the sending-end region at time t; $\Delta^{up}_{G,s,n'}$ and $\Delta^{down}_{G,s,n'}$ indicate the maximum upward and downward rate of thermal power unit n' in the sending-end region.

The actual output of renewable energy units is required to remain within the forecasted output range, which is expressed as:

$$0 \leqslant P_{NEG,n''}(t) \leqslant P^{pred}_{NEG,n''}(t) \tag{31}$$

3.2.2.2. Constraints on the transmission network. The power balance constraint is characterized by:

$$\boldsymbol{M}_{NG-i,s} \boldsymbol{P}_{NG,s}(t) + \boldsymbol{M}_{G-i,s} \boldsymbol{P}_{G,s}(t) - \boldsymbol{P}_{TL,s}(t) - \boldsymbol{P}_{ES,s}(t) = \boldsymbol{P}_{Load,s}(t) + \boldsymbol{M}_{l-i,s} \boldsymbol{P}_{l,s}(t) \tag{32}$$

where $\boldsymbol{P}_{NEG,s}(t)$, $\boldsymbol{P}_{G,s}(t)$, $\boldsymbol{P}_{TL,s}(t)$, $\boldsymbol{P}_{Load,s}$ (t) and $\boldsymbol{P}_{l,s}$ (t) represent the renewable energy output matrix, thermal power unit output matrix, tie-line transmission power matrix, node load power matrix, and line power flow matrix of the sending-end region at time t; $\boldsymbol{P}_{ES,s}(t)$ denotes the ES charging and discharging power matrix at time t; $\boldsymbol{M}_{NG\text{-}i,s}$, $\boldsymbol{M}_{G\text{-}i,s}$ and $\boldsymbol{M}_{l\text{-}i,s}$ are the renewable energy-node incidence matrix, thermal power unit-node incidence matrix and node-branch incidence matrix of the sending-end region.

The actual tie-line transmission capabilities are first constrained by the DFR boundaries. The DFR characterized for each time subset T_n can be transformed into the corresponding linear constraint set C_{Tn}, which can be expressed as:

$$\begin{cases} \boldsymbol{A}_{T_n}\boldsymbol{P}_{TL,T_n} \leqslant \boldsymbol{b}_{T_n}, \\ \boldsymbol{P}_{TL,T_n} = \left[P_{TL1,T_n^1}, \ldots, P_{TLN,T_n^1}, P_{TL1,T_n^2}, \ldots, P_{TLN,T_n^2}, \ldots, P_{TL1,T_n^m}, \ldots, P_{TLN,T_n^m}\right] \end{cases} \tag{33}$$

where $\boldsymbol{A}_{Tn}$ and $\boldsymbol{b}_{Tn}$ denote the coefficient matrix and constant term matrix of the linear constraints corresponding to the linear constraint set C_{Tn}.

Accordingly, the linear constraint set corresponding to the final DFR of tie-line transmission power can be expressed as:

$$C = \{C_1, C_2, \ldots, C_{Tn}\} \tag{34}$$

The actual tie-line transmission capability is subject to its own transmission limit:

$$-(1-\lambda_{tl})P_{TLn_l}^{\max} \leqslant P_{TLn_l}(t) \leqslant (1-\lambda_{tl})P_{TLn_l}^{\max} \tag{35}$$

where $P_{TLn_l}^{\max}$ denotes the transmission limit of the n_l-th tie-line. λ_{tl} represents the security margin.

In addition, the tie-line transmission power is constrained by ramp rate, which can be expressed as:

$$\begin{cases} P_{TLn_l}(t) - P_{TLn_l}(t-1) \leqslant \Delta_{TLn_l}^{\mathrm{up}} \\ P_{TLn_l}(t-1) - P_{TLn_l}(t) \leqslant \Delta_{TLn_l}^{\mathrm{down}} \end{cases} \tag{36}$$

where $\Delta_{TLn_l}^{\mathrm{up}}$ and $\Delta_{TLn_l}^{\mathrm{down}}$ are the maximum upward and downward rate of tie-line n_l.

3.2.2.3. Constraints on multi-type ES. Compared with the existing research in which ES types are predetermined, the proposed optimization model treats the ES configuration states as decision variables, which are introduced to couple the differentiated regulation boundaries of multi-type ES. The constraints associated with multi-type ES are given in Eqs. (1)–(4) of Section II (A). It should be noted that this study jointly incorporates multi-type ES configuration and operational constraints into both the DFR characterization model and the congestion management optimization model. The DFR characterization model provides feasible boundaries for the congestion management optimization model, while the congestion management optimization model supplies multi-type ES configuration schemes for the DFR characterization model. Through the iterative solution between the two models, the optimal configuration of multi-type ES and coordinated multi-resource dispatch strategies are achieved.

3.2.2.4. Constraints on DR. The constraint on response power of adjustable load is:

$$P_{adj,\min}(t) \leqslant P_{adj}(t) \leqslant P_{adj,\max}(t) \tag{37}$$

where $P_{adj,\max}(t)$ and $P_{adj,\min}(t)$ represent the upper and lower response power limits of adjustable load at time t.

The constraint on response power of reducible load is:

$$\begin{cases} P_{cut}(t) = (1-\theta(t))P_{cut^*}(t) \\ \theta(t)P_{cut^*}(t) \leqslant P_{cut^*}(t) - P_{cut}(t) \leqslant P_{cut^*}(t) \end{cases} \tag{38}$$

where $\theta(t)$ represents the load reduction coefficient at time t, indicating the reduction degree of the reducible load, with a value ranging from 0 to 100%.

The constraint on the response power of transferable load is:

$$P_{trans,\min}(t) \leqslant P_{trans}(t) \leqslant P_{trans,\max}(t) \tag{39}$$

where $P_{trans,\max}(t)$ and $P_{trans,\min}(t)$ are the upper and lower response power limits of transferable load at time t.

Transferable load is required to keep its electricity consumption constant during the dispatch cycle, which satisfy:

$$\sum_{t=1}^{T}(P_{trans'}(t) - P_{trans}(t)) = 0 \tag{40}$$

The constraint on response rate of DR is as shown in Eq. (11) of Section II (A).

3.3. Summary of the optimization strategy for congestion management based on MILP

Based on the linearization process, the optimization strategy for congestion management can be converted into an MILP model mathematically expressed as (39). This MILP model can be effectively solved by employing commercial solvers such as Gurobi.

$$\begin{aligned} &obj \max_{\mathrm{C,B}}(23) \\ &s.t.\ (1)-(4),(11),(30)-(40) \\ &\mathrm{C} = \left\{P_{G,s,n'}(t), P_{NEG,n''}(t), P_{TLn_l}(t), P_{adj}(t), P_{cut}(t), \right. \\ &\left. P_{trans}(t), P_{ES,k}^{\mathrm{N}}, E_{ES,k}^{\mathrm{N}}, P_{ch,k}(t), P_{dis,k}(t), SOC_k(t)\right\} \\ &\mathrm{B} = \left\{\lambda_k^i, \beta_{ch,k}(t), \beta_{dis,k}(t)\right\} \end{aligned} \tag{41}$$

where **C** and **B** are the set of continuous and binary variables, respectively.

4. Case study

In this section, case studies are conducted to validate our proposed approach. First, the comparative cases are introduced. Subsequently, the results and relevant discussions concerning the optimal configuration of multi-type ES, coordinated multi-resource dispatch strategy, tie-line transmission power, renewable energy accommodation and economic benefits, are further presented.

4.1. Case descriptions

To demonstrate the feasibility and effectiveness of the proposed DFR characterization approach, the optimization models of vertex search method and MILP based congestion management are run on MATLAB 2021 employing Gurobi with an Intel Core i5-12400 CPU. The proposed approach is validated on both the renewable-dominant cross-regional grid system in northern China and the IEEE 30-IEEE 39 interconnected test system to verify its applicability under different network topologies and system scales. The topology of the real-world system is shown in Fig. 5, which mainly consists of the sending-end system, the receiving-end system and two cross-regional tie-lines. The renewable energy generation and total load data of the sending-end system are presented in Fig. 6. And the basic parameters of Li-B, CAES, and PHS are shown in Table 2.

Combined with existing research, DFR can be summarized and classified into the following four methods. **M1**: DFR characterization excluding ES while incorporating N-1 security constraints; **M2**: DFR

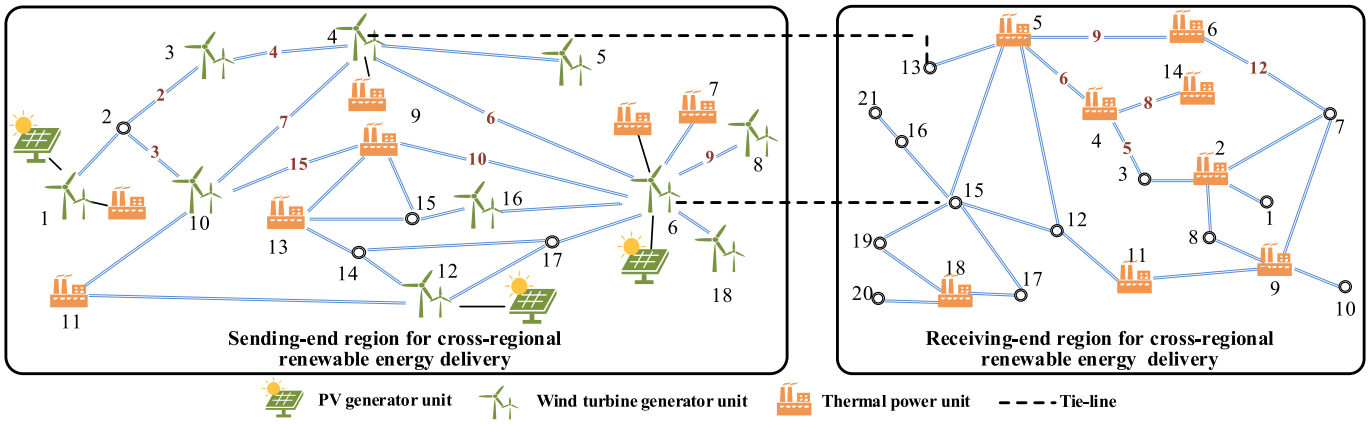

Fig. 5. Topology of the renewable-dominant cross-regional grids in northern China.

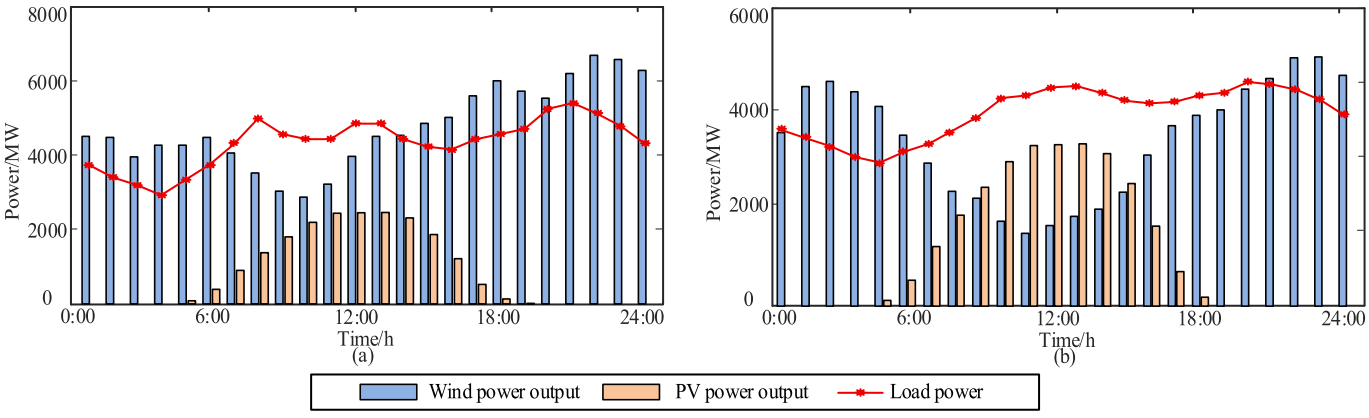

Fig. 6. Schematic of renewable energy and load in the sending-end region: (a) schematic of renewable energy and load in the real-world system; (b) schematic of renewable energy and load in the test system.

Table 2
Basic parameters of multi-type ES.

Parameters	Li-B	CAES	PHS
Initial SOC	0.5	0.5	0.5
Service life $T_{ES,\,k}$ (unit: year)	10	20	30
Discount rate	6%	6%	6%
Cycle efficiency	90%	70%	75%
Unit power investment cost (unit: 10^4 $)	17.15	78.43	91.04
Unit capacity investment cost (unit: 10^4 $)	11.20	6.31	9.80
Unit power operation and maintenance cost (unit: 10^4 $)	6.30	1.40	2.80

characterization considering single-type ES regulation alongside N-1 security constraints; **M**3: DFR characterization considering multi-type ES regulation but neglecting N-1 security constraints; **M**4: DFR characterization integrating multi-type ES regulation and N-1 security constraints. To validate the feasibility and effectiveness of proposed approach, several different cases are conducted as follows:

Case 1: The **M**1 method is adopted, without ES configured to be involved in system regulation.
Case 2: The **M**1 method is adopted, with single-type ES configured to be involved in system regulation.
Case 3: The **M**2 method is adopted, with single-type ES configured to be involved in system regulation.
Case 4: The **M**1 method is adopted, with multi-type ES configured to be involved in system regulation.
Case 5: The **M**3 method is adopted, with multi-type ES configured to be involved in system regulation.
Case 6: The **M**4 method is adopted, with multi-type ES configured to be involved in system regulation.

4.2. *Characterization results of the DFR*

In this paper, nodes 4 and 6 in the sending-end region and nodes 13 and 15 in the receiving-end region of the real-world system serve as tie-line nodes, as shown in the network topology. And nodes 4 and 10 in the IEEE 30 and nodes 5 and 16 in the IEEE 39 of the test system serve as tie-line nodes. The security operation spaces of two regional power grids are separately projected onto the two-dimensional space spanned by tie-line transmission power associated with these nodes to characterize the FRs at different times. Then, the intersection of two DFRs is performed to delineate renewable energy delivery boundaries. The scheduling horizon is set to 24 h with a time scale of 1 h. Fig. 7 (a) illustrates the characterization result of FR at 1:00. The FR contracts to ensure secure operation in various line contingency scenarios considering line N-1 security constraints. Without ES configuration, the FR characterized using **M**1 method is significantly constrained by the regulation capabilities of conventional power supplies and line transmission limits in cases 1,2, and 4, resulting in a relatively small region. In contrast, the regulation capability of ES is incorporated in cases 3 and 6, which expands the characterized FRs using **M**2 and **M**4 methods. Meanwhile, the final intersected FR is primarily constrained by the FR which is defined by the security constraints of receiving-end region, leading to identical boundaries in the first quadrant for cases 3 and 6. As a result, the FRs characterized using the M4 method integrated with ES regulation in the real-world system and the test system exhibit area expansions of 23.1%

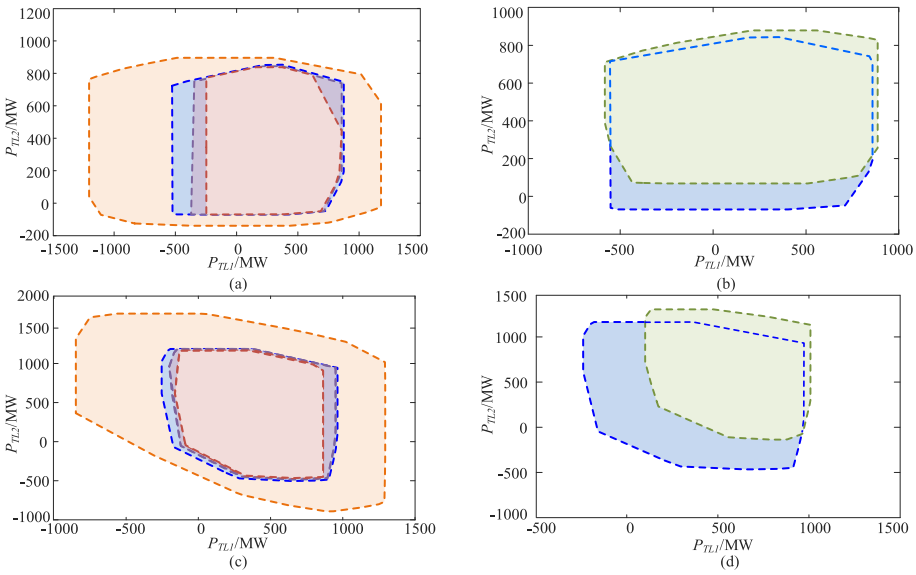

Fig. 7. The characterization results of FR: (a) characterization results of FR in the real-world system at 01:00; (b) schematic of FR comparison at 01:00 and 10:00 in the real-world system; (c) characterization results of FR in the test system at 01:00; (d) schematic of FR comparison at 01:00 and 10:00 in the test system.

and 6.2%, compared with the M1 method at 01:00. Across all time steps, the average DFR areas increase by 33.6% and 20.3%, respectively. Moreover, the DFR characterized using **M**3 method which does not incorporate line N-1 security constraints is larger than those from other methods, while encompassing tie-line transmission power combinations resulting in congestion, particularly in line contingency scenarios.

Coordinated constraints on the transmission power of multiple tie-lines are imposed by the internal power flow distribution and energy transfer characteristics in the regional power grid, yielding an irregularly shaped FR. A comparison of FRs at 01:00 and 10:00 in case 6 is shown in Fig. 7 (b) and (d). The results indicate pronounced differences across time points in terms of the boundaries and areas of FRs. The real-time boundaries of cross-regional renewable energy delivery can be explicitly identified by characterizing the FR on an hourly basis, thereby supporting the line congestion management.

In the proposed iterative optimization framework integrating DFR characterization and congestion management optimization, the total computational time can be decomposed into two main components, namely the DFR characterization time (I) and the congestion management optimization time (II) at each iteration. Parallel computation is adopted for handling line N-1 contingency scenarios. For the case study on the real-world system, three iterations are performed, resulting in an overall computational time of 2733 s. The average computation time for DFR characterization is 871 s, while the average solution time of the congestion management optimization model is 40 s. The detailed breakdown is provided in the Table 3.

The proposed approach integrates DFR characterization with congestion management in an iterative coordination optimization framework, and the computation efficiency of DFR characterization significantly influences the overall solution time. To evaluate its efficiency, additional comparisons are conducted under different system scales, time steps, and numbers of tie-lines, as shown in Table 4. Specifically, IEEE 30 bus system and IEEE 118 bus system are adopted for system-scale analysis. Moreover, in the real-world system, the number of tie-lines is set to 1, 2, and 3 under a 60-min time step. Furthermore, time-step sensitivity is evaluated under 15-min, 30-min, and 60-min time steps with two tie-lines. The results indicate that the computation time increases with larger system scales, more tie-lines, and shorter time steps. In particular, an increase in the number of tie-lines leads to a higher-dimensional projection of the low-dimensional time subset, which significantly increases the computation burden of vertex search in the DFR characterization.

Table 3
The breakdown of computational time.

	The first iteration	The second iteration	The third iteration	Total/s
Part I/s	870	865	878	/
Part II/s	41	41	38	/
Total/s	911	906	916	2733

Table 4
Comparison of computational time.

System	Number of transmission lines	Number of tie-lines	Time step/min	Computation time/s
The real-world system	25	1	60	132
	25	2	15	3150
			30	1635
			60	871
	25	3	60	6558
IEEE 30 bus system	41	2	60	1369
IEEE 118 bus system	186	2	60	5124

In the proposed framework, the error tolerance is adopted to evaluate the approximation accuracy of boundary segments. A smaller tolerance leads to finer boundary refinement and larger characterized DFR areas by capturing more actual feasible boundary regions, while also increasing the computational burden. To analyze this trade-off, a sensitivity analysis of FR area and computation time under different error tolerances at 20:00 is conducted in Table 5. In this study, an error tolerance of 10 is selected. Compared with the case of tolerance equal to 1, the characterization accuracy decreases by only 0.72%, while the computation time is reduced by 11.0%. Therefore, an error tolerance of 10 achieves a favorable balance between computational efficiency and FR characterization accuracy.

The feasibility of the adopted time decomposition strategy is validated by comparing the computational time and solution accuracy of three different solution strategies, as shown in Table 6. Through comparative analysis of the projected FR at time 01:00, it can be observed that Method A1, which fully considers multi-period temporal

Table 5
Sensitivity analysis of FR area and computation time under different error tolerances.

Error tolerances	30	20	10	1	0.1
FR area/MW^2	1198783.8154	1218814.1281	1220959.3505	1229827.0227	1230025.1435
computation time/s	656	816	871	979	1120

Table 6
Comparison of computational time and solution accuracy among different strategies.

Methods	Multi-period temporal coupling constraints	Computation time/s	Characterization accuracy
A1	Full coupled high-dimensional strategy	> 10000	100%
A2	Decoupled strategy	26.8	77.42%
A3	Time decomposition strategy	871	95.57%

coupling constraints, suffers from excessively high projection dimensionality. When the vertex search method is employed, the number of vertices to be identified increases dramatically, resulting in a computation time exceeding 10000 s. In contrast, Method A2 neglects temporal coupling constraints, significantly reducing the computation time to only 26.8 s, but yielding a relatively low characterization accuracy of 77.42%. Method A3, however, adopts a time decomposition strategy, enabling the characterization of a highly accurate FR within a reasonable computation time.

4.3. Analysis of optimal ES configuration results

The optimization results of multi-type ES configuration are analyzed based on the real-world system in this subsection. A single-type of Li-B is configured in cases 2 and 3 to be jointly involved in system regulation incorporating DR and thermal power units, while multi-type ES including Li-B, CAES, and PHS is configured in cases 4, 5, and 6. The optimal configurations of ES are obtained by solving the MILP-based model, which are represented in Table 7.

The complementary regulation capabilities of different ESs can be fully leveraged with configuring the multi-type ES in case 4 compared with case 2, leading to a 15.3% reduction in the configured rated power of ES. Similarly, the configured rated power in case 6 is reduced by 17.6% relative to case 3. Similar conclusions can also be observed in the test system, where the configured rated power in cases 6 and 4 is reduced by 8.6% and 17.5% compared with cases 2 and 3. In addition, the configured rated power in case 5 differs only slightly from that in case 6. However, the DFR in case 5 is characterized using the M3 method without considering N-1 security constraints, resulting in a larger delivery boundary than that obtained in case 6 and significantly increasing the system operation risk.

Table 7
Optimal configuration results of ES in cases 2–6.

Case 2	Configuration type	Li-B					
	Node	1	8	10	11	14	15
	Rated power (MW)	177	180	100	180	180	180
	Rated capacity (MWh)	710	720	400	720	720	720
Case 3	Configuration type	Li-B					
	Node	1	8	9	11	12	13
	Rated power (MW)	121	180	240	180	206	146
	Rated capacity (MWh)	400	720	720	720	720	583
Case 4	Configuration type	Li-B		CAES			PHS
	Node	3	17	1	8	18	5
	Rated power (MW)	131	119	135	150	149	160
	Rated capacity (MWh)	411	400	810	1200	897	1600
Case 5	Configuration type	Li-B		CAES			PHS
	Node	2	11	4	8	10	5
	Rated power (MW)	133	191	127	150	150	154
	Rated capacity (MWh)	400	575	765	1200	900	1544
Case 6	Configuration type	Li-B		CAES			PHS
	Node	10	11	2	6	8	5
	Rated power (MW)	170	170	102	150	150	142
	Rated capacity (MWh)	510	536	614	900	1200	1422

4.4. Analysis of cross-regional renewable energy delivery operation results

The cross-regional renewable energy delivery operation results are analyzed based on the real-world system in this subsection. The diagrams of power balance in cases 1 to 6 are shown in Fig. 8. During periods of high renewable generation, renewable energy accommodation is enhanced by increasing flexible loads within their regulation limits and absorbing surplus power through ES. During low renewable generation periods, the tie-line utilization is increased by reducing flexible loads, ES discharging and increasing the output of thermal power units to get higher cross-regional delivery power revenues.

Comparison of cases 1, 2, 3, 4, and 6 highlights the effectiveness of the proposed DFR characterization approach in enhancing the delivery power, improving the renewable energy accommodation. The comparison between cases 5 and 6 further demonstrates that the approach effectively prevents line flow violations in the regional grid and avoids the occurrence of system imbalanced power. Specifically, DFRs are characterized using the **M**1 method in cases 2 and 4. In case 4, multi-type ES is configured, allowing the complementary regulation capabilities of different ESs to be fully leveraged. Compared with case 2, the delivery power and renewable energy accommodation rate in case 4 increase by 0.06% and 0.76%, respectively. Meanwhile, the pressure on DR regulation is alleviated by configuring multi-type ES, leading to a 5.5% reduction of the response power. Similarly, DFRs in cases 3 and 6 are characterized using the **M**2 and **M**4 methods, producing identical results. Compared with case 3, case 6 with multi-type ES configured achieves increases of 0.60% and 0.74% in delivery power and renewable energy accommodation rate, while the response power of DR is reduced by 6.5%, demonstrating the advantages of multi-type ES. Fig. 9 illustrates the charging-discharging power and SOC operation of the ES in case 6 to analyze the complementary regulation process of multi-type ES. The Li-Bs exhibit high charging-discharging power but are limited in continuous operation duration, while the CAESs and PHS provide stable charging-discharging power over extended periods. Through their coordinated complementary operation, the overall regulation performance and operational flexibility of the system are significantly enhanced. Moreover, multi-type ES is configured in cases 4 and 6, while the DFR is characterized using the **M**1 and **M**4 methods, respectively. As shown in Fig. 7, the DFR characterized using the **M**4 method is larger than using **M**1 method, significantly expanding the adjustable range of tie-line transmission power in case 6 compared with case 4, and yielding increases of 5.7% and 0.02% in delivery power and renewable energy accommodation rate. In particular, the DFR in case 5 is characterized using the **M**3 method without incorporating the line N-1 security constraints, leading to a larger delivery boundary relative to case 6. Consequently, the delivery power in case 5 is slightly higher than that in case 6, resulting in combinations of tie-line transmission power which pose congestion risks to the receiving-end region.

The necessity of considering line N-1 security constraints is analyzed

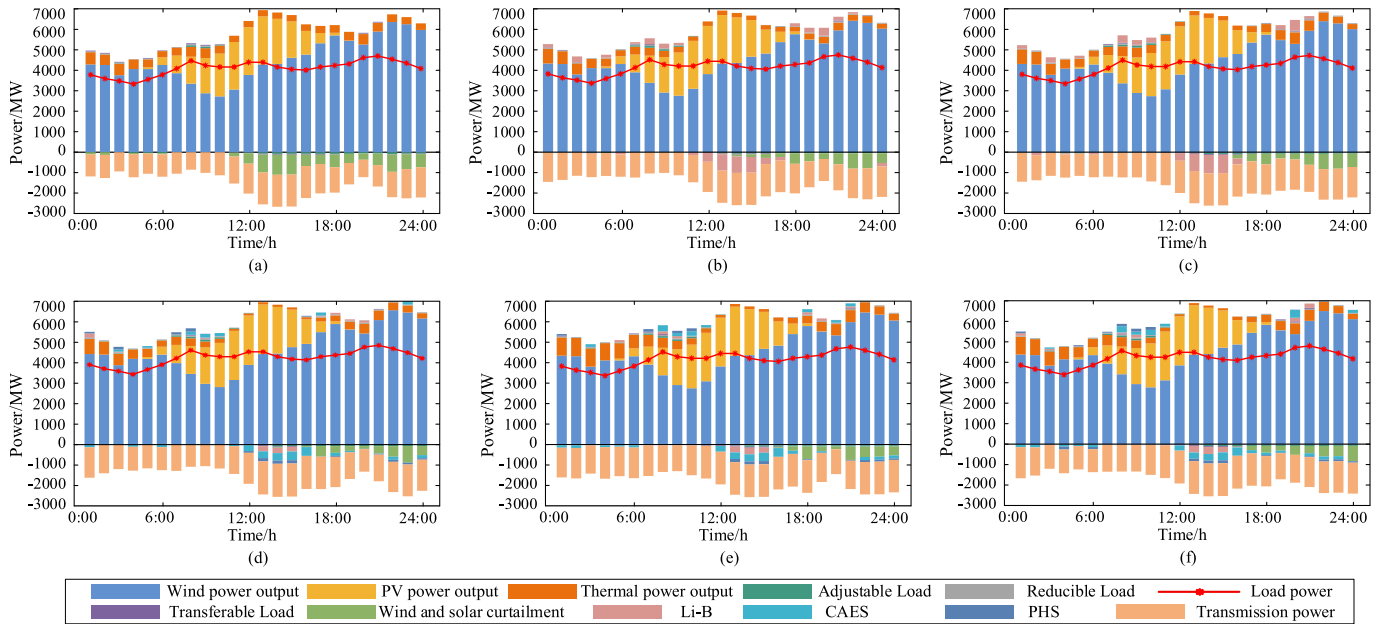

Fig. 8. Schematic of power balance in the real-world system: (a) schematic of power balance in case 1; (b) schematic of power balance in case 2; (c) schematic of power balance in case 3; (d) schematic of power balance in case 4; (e) schematic of power balance in case 5; (f) schematic of power balance in case 6.

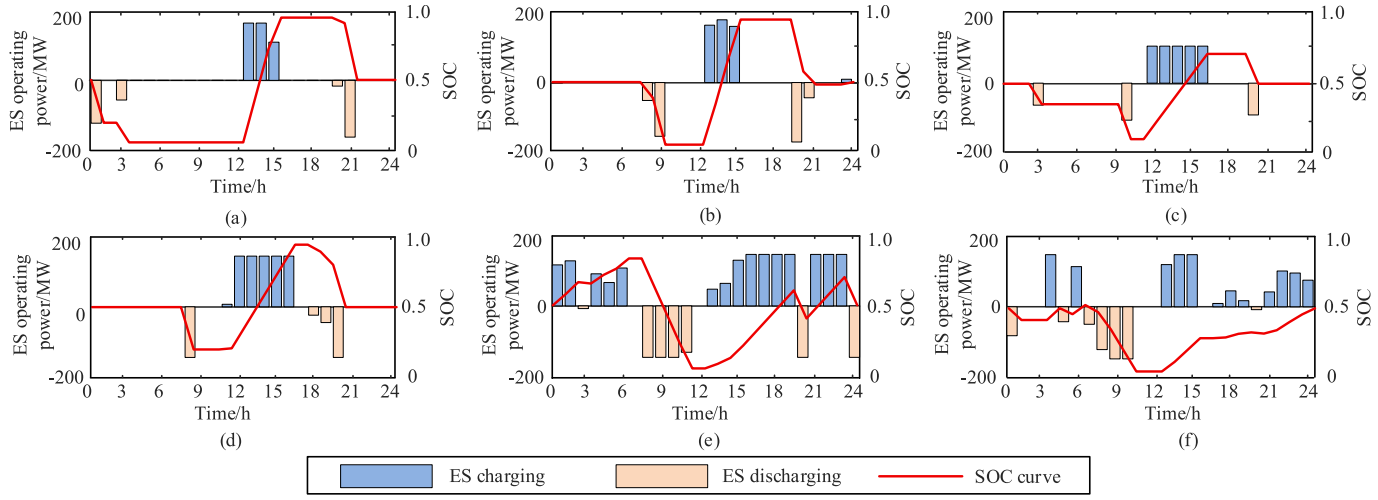

Fig. 9. Operation power and SOC chart of ES in the real-world system in case 6: (a) operation power and SOC chart of Li-B at node 10; (b) operation power and SOC chart of Li-B at node 11; (c) operation power and SOC chart of CAES at node 2; (d) operation power and SOC chart of CAES at node 6; (e) operation power and SOC chart of CAES at node 8; (f) operation power and SOC chart of PHS at node 5.

from the perspective of power flows on the transmission lines in the receiving-end regional power grid. In the real-world system, supposing that a contingency occurs on line 5 at the initial time for each case, the power flow originally carried by line 5 is then redistributed to lines 6, 8, and other lines. Fig. 10 illustrates the power flow of line 8 in the real-world system. In case 5, the power flow violations are observed during 05:00–06:00, 13:00–19:00, and 21:00–23:00, with the maximum overload reaching 11.8%. Prolonged line overloading may trigger a trip, resulting in an interruption of the local power supply network. Similar conclusions can also be observed for line 7 in the receiving-end region of the test system.

The slack variable is introduced into the power balance constraint within the operation model of regional power grid to capture node imbalanced power while ensuring that all security constraints are satisfied. The node imbalanced power in the receiving-end regional power grid can be evaluated for different tie-line transmission power injection combinations by incorporating this slack variable into the penalty term of the objective function. As shown in Fig. 11, the node imbalanced power rises sharply when the combination of tie-line transmission power exceeds the DFR characterized with line N-1 security constraints. There is no node imbalanced power in cases 1–4 and case 6 with DFRs accounting for line N-1 security constraints. In contrast, a total node imbalanced power of 185.2 MW is generated to maintain stable grid operation in case 5 of the real-world system, while the corresponding imbalanced power in the test system reaches 340.1 MW.

The comparisons of total thermal power generation, delivery power and renewable energy curtailment for cases 1, 3, and 6 in the real-world system and the test system accounting for line N-1 security constraints are illustrated in Fig. 12 (a) and (b). There is a conflict between substantial renewable energy curtailment and low tie-line utilization in cases 1 and 3. This can be attributed to the limited flexibility of the

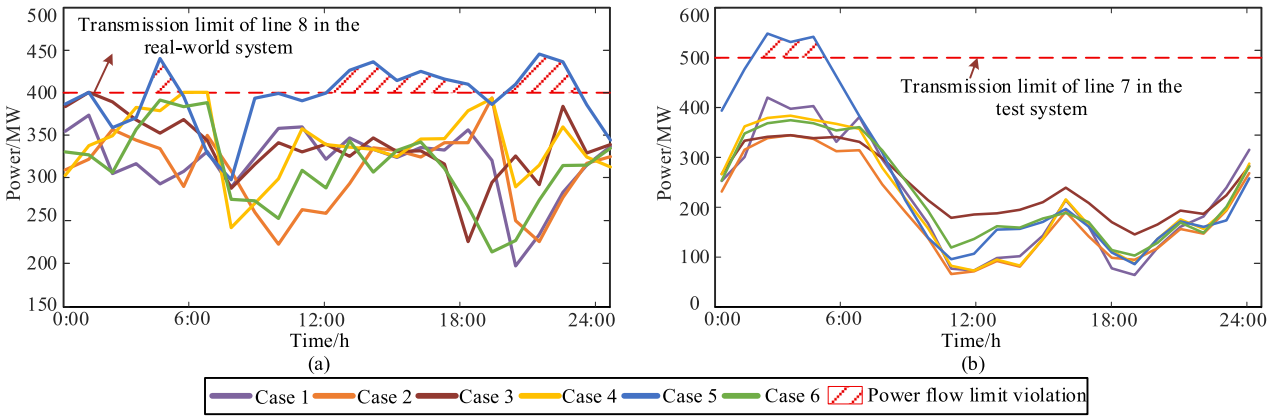

Fig. 10. Power flow in the receiving-end region in cases 1–6: (a) power flow of line 8 in the receiving-end region of the real-world system; (b) power flow of line 7 in the receiving-end region of the test system.

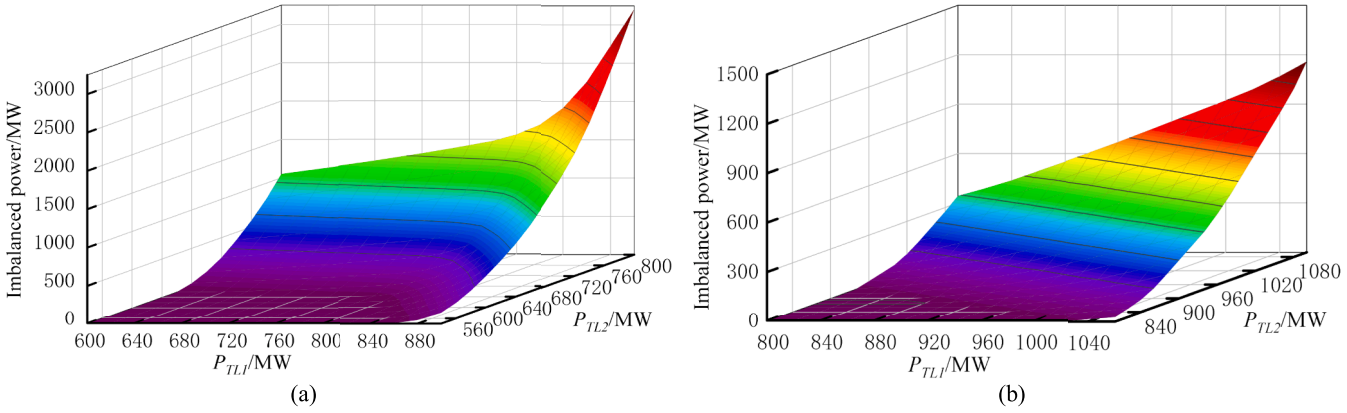

Fig. 11. Schematic of node imbalanced power: (a) schematic of node imbalanced power in the real-world system; (b) schematic of node imbalanced power in the test system.

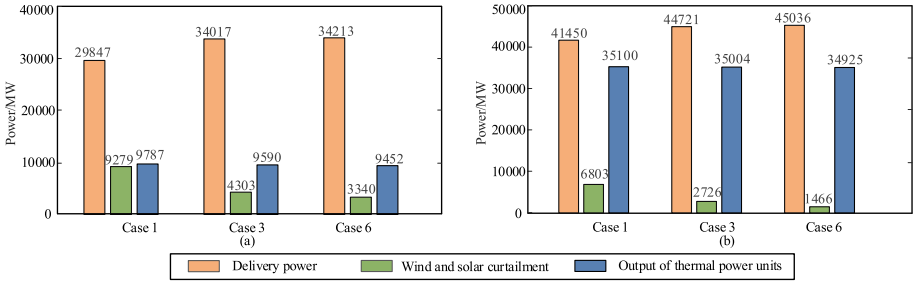

Fig. 12. Comparisons of total thermal power generation, transmission power and wind and solar curtailment: (a) comparisons of total thermal power generation, transmission power and wind and solar curtailment in the real-world system; (b) comparisons of total thermal power generation, transmission power and wind and solar curtailment in the test system.

system with no ES or only a single type of ES configured. As a result, line congestion frequently occurs in the sending-end regional power grid, preventing surplus renewable energy from effectively reaching the tie-line nodes. At the same time, there is a conflict between substantial renewable energy curtailment and elevated output of thermal power units in cases 1 and 3, which is due to renewable energy failing to reach high-demand nodes, forcing nearby thermal power units to compensate. In contrast, the regulation potential of flexible resources is fully exploited in case 6, which further alleviates line congestion by improving power flow distribution, thereby effectively resolving the above conflicts.

Fig. 13 illustrates the comparison of partial line loading rates in cases 1, 3, and 6 at 14:00 when renewable energy generation reaches its peak and line congestion is more likely to occur. As shown in Fig. 13 (a), in the real-world system, lines 3, 4, and 9 operate at full load in case 1. By contrast, the power on lines 3 and 4 is redistributed to other lightly loaded lines with the regulation of single-type ES in case 3, thereby reducing their loading rates. Additionally, congestion on these lines is fully alleviated with multi-type ES configured in case 6, which provides the strongest regulation capability. Consistent observations can also be identified in the test system.

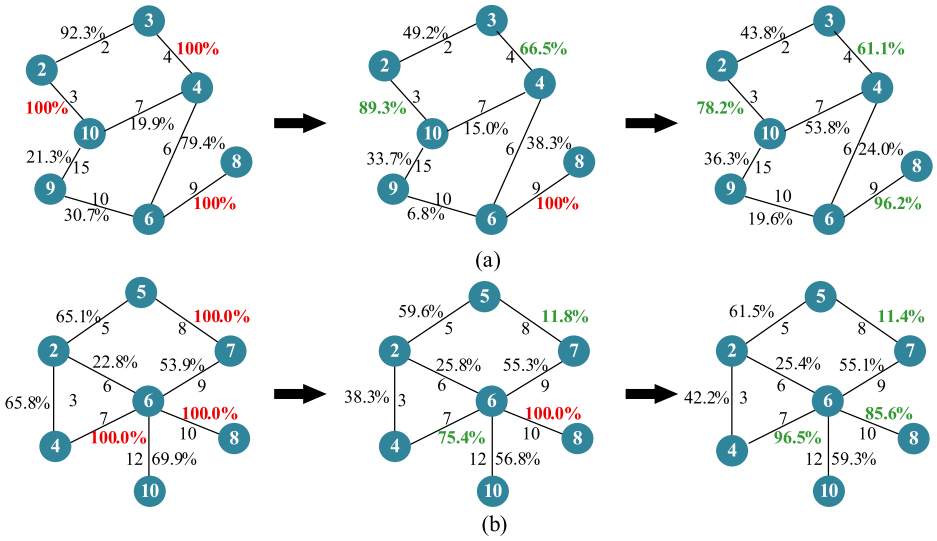

Fig. 13. Schematic of partial line loading rate comparisons for cases 1, 3, and 6 at 14:00: (a) schematic of partial line loading rate comparisons in the real-world system; (b) schematic of partial line loading rate comparisons in the test system.

4.5. Analysis of economic performance

4.5.1. Comparative analysis of economic indicators

In this subsection, the economic superiority of the proposed approach is demonstrated in terms of system costs and revenues. The economic benefit conditions in the real-world system are summarized in Table 8. Compared with cases 1–4, case 6 applies the M4 method to characterize the DFR, with multi-type ES configured to be jointly involved in system regulation incorporating DR and thermal power units, yielding increases of 33.3%, 9.1%, 8.0%, and 1.3% in comprehensive economic benefits, respectively. Meanwhile, the comprehensive economic benefit in case 6 remains 1.0% higher than case 5, which is mainly attributed to the inclusion of the imbalanced power penalty cost in case 5. In addition, compared with configuring the single-type ES, the complementary regulation advantages of different ESs are fully leveraged by configuring the multi-type ES. As a result, the regulation potential of the ES is more effectively released, leading to a 24.1% reduction in ES cost in case 6 relative to case 3. Moreover, the enhanced flexibility provided by multi-type ES reduces the reliance on DR for system regulation, thereby further decreasing the DR cost by 6.2% in case 6. Similar improvements in economic performance can also be observed in the test system, further verifying the effectiveness of the proposed approach in enhancing comprehensive economic benefits.

4.5.2. Sensitivity analysis of economic indicator weight coefficients

In the objective function (23) of the proposed congestion management optimization model, various economic indicators are aggregated to evaluate the overall system economic benefit through a linear weighting method. Since indicators such as tie-line delivery power, renewable energy curtailment, and ES cost are of comparable importance in dispatch decisions and no explicit priority relationship is defined, an equal-weight configuration is employed to construct the objective function in this paper. Specifically, all weighting coefficients are set to 1, i.e., $\lambda_1 = \lambda_2 = \lambda_3 = \lambda_4 = \lambda_5 = 1$. Furthermore, the rationality of the selected weighting coefficients is validated through sensitivity analysis.

A single-factor control method is adopted in this study. Taking the weighting configuration used in the manuscript as the benchmark case, each target weight is varied one at a time within a reasonable range while keeping the remaining weights unchanged. The core evaluation indicators include three key metrics in the manuscript, namely tie-line delivery power, renewable energy curtailment, and comprehensive economic benefits. These indicators can effectively reflect the impact of weight variations on both the technical and economic performance. The results of the sensitivity analysis (relative to the benchmark weighting setting) are presented in Table 9. The analysis results indicate that the benchmark weighting setting exhibits favorable robustness with respect to the three core evaluation indicators. Specifically, when λ_1 varies within the range of 0.8–1.2, the maximum variation in comprehensive economic benefit reaches approximately 60%. Meanwhile, the variation in tie-line delivery power remains within 9% when λ_1 ranges from 0.9 to 1.2. However, when λ_1 is reduced to 0.8, the tie-line delivery power decreases by 19.21% compared with the benchmark case. For λ_2, the variation in tie-line delivery power remains within approximately 9% when λ_2 varies from 0.8 to 1.1. Notably, when λ_2 increases to 1.2, the tie-

Table 8
Economic benefit conditions in cases 1–6 (unit: 10^4 $).

Case	Tie-line delivery power revenue	Wind and solar curtailment penalty cost	DR cost	ES Cost	Thermal power unit cost	Imbalanced power penalty cost	Comprehensive economic benefits
Case 1	418.1	65.0	11.9	0.0	116.5	0.0	224.6
Case 2	453.4	30.5	12.7	39.8	95.8	0.0	274.5
Case 3	476.5	30.1	13.0	41.9	114.3	0.0	277.2
Case 4	453.4	23.5	12.0	30.1	92.0	0.0	295.7
Case 5	504.1	23.4	12.6	31.5	133.6	6.7	296.3
Case 6	479.3	23.4	12.2	31.8	112.5	0.0	299.4

Table 9
Core results of sensitivity analysis.

Parameter	Weight coefficients setting	Tie-line delivery power	Renewable energy curtailment	Comprehensive economic benefits
λ_1	0.8	−19.21%	0.00%	−29.61%
	0.9	−4.04%	0.00%	−15.43%
	1.1	+1.68%	−1.50%	+16.14%
	1.2	+4.00%	−1.48%	+32.69%
λ_2	0.8	+4.27%	0.00%	+8.00%
	0.9	+2.33%	0.00%	+3.84%
	1.1	−4.05%	−1.50%	−3.55%
	1.2	−18.91%	−1.50%	−6.22%
λ_3	0.8	+3.45%	−1.61%	+2.53%
	0.9	+1.75%	−1.50%	+1.08%
	1.1	−0.64%	+1.14%	−1.26%
	1.2	−1.04%	+1.51%	−2.39%
λ_4	0.8	+0.04%	0.00%	+0.84%
	0.9	+0.04%	0.00%	+0.42%
	1.1	−1.22%	+1.25%	−0.51%
	1.2	−1.19%	+1.50%	−0.89%
λ_5	0.8	−0.03%	+1.50%	+1.45%
	0.9	−0.01%	+1.11%	+0.65%
	1.1	+0.03%	−1.42%	−0.89%
	1.2	+0.08%	−1.80%	−1.64%

line delivery power decreases by 18.91% compared with the benchmark case. In addition, when λ_3, λ_4, and λ_5 vary within the range of 0.8–1.2, the variations in all three evaluation indicators remain within 3.5% compared with the benchmark case. In summary, both the qualitative and quantitative conclusions of the study remain stable under reasonable weight perturbations, thereby validating the rationality of the adopted weighting setting.

5. Conclusions

This paper proposes a DFR characterization approach for tie-line transmission power considering the regulation capability of multi-type ES and line N-1 security constraints to support congestion management. An iterative coordination optimization strategy integrating DFR characterization and congestion management for renewable-dominant cross-regional power grids is further developed to exploit the potential of cross-regional resource allocation. The results indicate that:

(1) By incorporating multi-type ES as a regulation variable into the vertex search-based model of the DFR for tie-line transmission power in the studied real-world system, the original DFR is expanded, with an average increase of 33.6% in the area across all time steps. This expansion enlarges the adjustable range of tie-line transmission power and enhances renewable energy delivery capability.
(2) By employing an intersection calculation to incorporate N-1 security constraints, the DFR of tie-line transmission power is established to delineate the system's actual operation boundaries. In the studied real-world system, this methodological framework alleviates the risk of power flow violations with a maximum violation amount of up to 11.8%, thereby improving operational security.
(3) An optimization framework for congestion management is developed considering the refined regulation capability model of multi-type ES. In the studied real-world system, compared with the single-type ES configuration, the proposed model increases the renewable energy accommodation rate and delivery power by 0.74% and 0.60%, respectively, while improving the comprehensive economic benefits by 8.0%.

The proposed approach can characterize the DFR based on day-ahead forecast scenarios, while the required model inputs can all be obtained from practical dispatching system operations, thereby demonstrating a certain level of practical applicability. However, the real-time computational performance still requires further improvement. Meanwhile, to address the impact of uncertainty, future work may incorporate robust optimization or chance-constrained methods to explicitly model renewable energy forecast errors, thereby constructing robust or probabilistic DFRs. In addition, the general applicability to larger-scale power grids and more diverse operating scenarios remains to be further investigated.

CRediT authorship contribution statement

Zhengyang Xu: Writing – review & editing, Writing – original draft, Visualization, Supervision, Software, Project administration, Methodology, Investigation, Formal analysis, Data curation, Conceptualization. **Jie Li:** Writing – review & editing, Writing – original draft, Software, Resources, Methodology, Formal analysis, Data curation, Conceptualization. **Zixuan Zheng:** Writing – original draft, Supervision, Resources, Methodology, Formal analysis, Data curation. **Chunjun Huang:** Visualization, Validation, Supervision, Methodology. **Zheng Ren:** Writing – review & editing, Visualization, Supervision, Methodology, Data curation. **Guozheng Shang:** Visualization, Validation, Supervision, Resources, Methodology. **Yuntao Sun:** Writing – original draft, Resources, Formal analysis, Data curation. **Weiwei Miao:** Supervision, Methodology, Funding acquisition, Data curation. **Ning Zhou:** Visualization, Supervision, Resources, Funding acquisition. **Yuanzhen Zhu:** Visualization, Validation, Supervision.

Declaration of competing interest

The authors declare that they have no known competing financial interests or personal relationships that could have appeared to influence the work reported in this paper.

Acknowledgments

This work was supported by the National Natural Science Foundation of China under Grant 52277115.

Data availability

Data will be made available on request.

References

[1] Liao F, Liang Y, Zhou C, Fan B, Qin Q. A multi-scale model for renewable portfolio standard-driven provincial energy planning in China. Renew Energy 2025;254:123654. https://doi.org/10.1016/j.renene.2025.123654.
[2] Zhang Z, Wang Y, Wang C, Su Y, Wang Y, Yong D. Distributed chance-constrained optimal dispatch for integrated energy system with electro-thermal couple and wind-storage coordination. IEEE Trans Ind Appl 2025;61(1):833–46. https://doi.org/10.1109/TIA.2024.3472653.
[3] Liu B, Liu T, Liao S, Lu J, Cheng C. Short-term coordinated hybrid hydro-wind-solar optimal scheduling model considering multistage section restrictions. Renew Energy 2023;217:119160. https://doi.org/10.1016/j.renene.2023.119160.
[4] Yang J, Yang M, Ma K, Dou C, Ma T. Distributed optimization of integrated energy system considering demand response and congestion cost allocation mechanism. Int J Electr Power Energy Syst 2024;157:109865. https://doi.org/10.1016/j.ijepes.2024.109865.
[5] Zhang T, Li G, Wang J, Wei W, Zhou M. Coordinated operation method of renewable energy power systems based on feasible region projection theory. Trans China Electrotech Soc 2024;39(09):2784–96. https://doi.org/10.19595/j.cnki.1000-6753.tces.230196.
[6] Dehghan S, Amjady N. Robust transmission and energy storage expansion planning in wind farm-integrated power systems considering transmission switching. IEEE

Trans Sust Energy 2016;7(2):765–74. https://doi.org/10.1109/TSTE.2015.2497336.
[7] Li S, Wang L, Gu X, Zhao H, Sun Y. Optimization of loop-network reconfiguration strategies to eliminate transmission line overloads in power system restoration process with wind power integration. Int J Electr Power Energy Syst 2022;134:107351. https://doi.org/10.1016/j.ijepes.2021.107351.
[8] Valipour E, Nourollahi R, Tarafdar Hagh M, Zare K, Ghassem ZS. Boosting renewable hosting capacity via TCSC-enhanced transmission system planning: P-robust stochastic approach. Renew Energy 2026;258:124922. https://doi.org/10.1016/j.renene.2025.124922.
[9] Zhu J, Wang J, Zheng Y, Zhang X, Liu X, Wang X, et al. Two-stage coevolutionary constrained multi-objective optimization algorithm for solving optimal power flow problems with wind power and FACTS devices. Renew Energy 2024;232:121087. https://doi.org/10.1016/j.renene.2024.121087.
[10] Huang J, Du Z, Yu Y, Zhao H, Chen Y. A two-layer optimal dispatch model for thermal unit deep peaking shaving and dynamic line rating. Int J Electr Power Energy Syst 2025;172:111098. https://doi.org/10.1016/j.ijepes.2025.111098.
[11] Sadeghian O, Mohammadi-Ivatloo B. Chance-constrained dynamic thermal line rating of power system for enhancing stochastic renewable penetration. Renew Energy 2026;256:124030. https://doi.org/10.1016/j.renene.2025.124030.
[12] Li X, Wang W, Wang H, Wu J, Xu Q. Flexibility robust optimal operation strategy for cross-regional interconnected power under load-source coordination. IEEE Access 2020;8:161124–37. https://doi.org/10.1109/ACCESS.2020.3020646.
[13] Chen S. Measuring regional variations and analyzing determinants for global renewable energy. Renew Energy 2025;244:122644. https://doi.org/10.1016/j.renene.2025.122644.
[14] Tie Y, Hu B, Shao C, Huang W, Qi F, Xie K. Integrated flexibility characterization and measurement of distributed multi-energy systems considering temporal coupling constraints. Energy 2023;283:128684. https://doi.org/10.1016/j.energy.2023.128684.
[15] Liu J, Chu C. Iterative distributed algorithms for real-time available transfer capability assessment of multiarea power systems. IEEE Trans Smart Grid 2015;6(5):2569–78. https://doi.org/10.1109/TSG.2015.2388777.
[16] Yu J, Liu J, Li W, Xu R, Yan W, Zhao X. Limit preserving equivalent method of interconnected power systems based on transfer capability consistency. IET Gener Transm Distrib 2016;10:3547–54. https://doi.org/10.1049/iet-gtd.2016.0254.
[17] Sun Y, Ding T, Qu M, Wang F, Shahidehpour M. Interval total transfer capability for mesh HVDC systems based on sum of squares and multi-dimensional holomorphic embedding method. IEEE Trans Power Syst 2022;37(6):4157–67. https://doi.org/10.1109/TPWRS.2022.3145065.
[18] Jang W, Overbye T. Equivalent line limit calculation using available thermal transfer capability. In: 2017 IEEE Texas Power and Energy Conference (TPEC); 1-6. doi: 10.1109/TPEC.2017.7868287.
[19] Lin W, Yang Z, Yu J, Jin L, Li W. Tie-line power transmission region in a hybrid grid: fast characterization and expansion strategy. IEEE Trans Power Syst 2020;5(3):2222–31. https://doi.org/10.1109/TPWRS.2019.2950906.
[20] Lin W, Yang Z, Yu J, Yang G, Wen L. Determination of transfer capacity region of tie lines in electricity markets: theory and analysis. Appl Energy 2019;269:1441–58. https://doi.org/10.1016/j.apenergy.2019.01.146.
[21] Dai W, Yang Z, Yu J, Zhao K, Wen S, Lin W, et al. Security region of renewable energy integration: characterization and flexibility. Energy 2019;187:115975. https://doi.org/10.1016/j.energy.2019.115975.
[22] Liu S, Yang Z, Xia Q, Lin W, Shi L, Zeng D. Power trading region considering long-term contract for interconnected power networks. Appl Energy 2020;261:114411. https://doi.org/10.1016/j.apenergy.2019.114411.
[23] Che B, Wen S, Dong X, Yu J, Qi C, Dai W. Feasible region of transmission sections: weak factors identification and expansion. IEEE Access 2020;8:90099–108. https://doi.org/10.1109/ACCESS.2020.2993869.
[24] Tan Z, Zhong H, Wang J, Xia Q, Kang C. Enforcing intra-regional constraints in tie-line scheduling: a projection-based framework. IEEE Trans Power Syst 2019;34(6):4751–61. https://doi.org/10.1109/TPWRS.2019.2913876.
[25] Tan Z, Yan Z, Zhong H, Xia Q. Non-iterative solution for coordinated optimal dispatch via equivalent projection-Part II: Method and applications. IEEE Trans Power Syst 2023;39(1):899–908. https://doi.org/10.1109/TPWRS.2023.3257033.
[26] Huang X, Guo C, Zhang J, Meng F, Zhang J. Study on the impact of grid-following and grid-forming storage on the power transmission capacity of wind-solar-hydro bundled system via LCC-HVDC transmission. Proc CSEE 2025:1–14. https://link.cnki.net/urlid/11.2107.TM.20251107.0920.004.
[27] Xiao Q, Zhou J, Fan X, Shao X, Zhou Q, Qu S, et al. Tie-line exchange capability considering N-1 constraints: characterization and analysis. J Chong Univ 2023;48(09):12–20. https://doi.org/10.11835/j.issn.1000-582X.2024.216.
[28] Lin W, Zhao C. Cost functions over feasible power transfer regions of virtual power plants. IEEE Syst J 2023;17(2):2950–60. https://doi.org/10.1109/JSYST.2022.3198278.
[29] Lin W, Yang Z, Yu J, Xie K, Wang X, Li W. Tie-line security region considering time coupling. IEEE Trans Power Syst 2021;36(2):1274–84. https://doi.org/10.1109/TPWRS.2020.3015483.
[30] Zhang T, Wang J, Li G, Wang X, Zhou M. Characterizing temporal-coupled feasible region of active distribution networks. IEEE Trans Ind Appl 2022;58(5):5687–96. https://doi.org/10.1109/TIA.2022.3180704.
[31] Zhang T, Wang J, Wang H, Jin R, Li G, Zhou M. On the coordination of transmission-distribution grids: a dynamic feasible region method. IEEE Trans Power Syst 2023;38(2):1857–68. https://doi.org/10.1109/TPWRS.2022.3197556.
[32] Lin W, Jiang H, Jian H, Xue J, Wu J, Wang C, et al. High-dimension tie-line security regions for renewable accommodations. Energy 2023;270:126887. https://doi.org/10.1016/j.energy.2023.126887.
[33] Chen X, Anese E, Zhao C, Li N. Aggregate power flexibility in unbalanced distribution systems. IEEE Trans Smart Grid 2019;11(1):258–69. https://doi.org/10.1109/TSG.2019.2920991.
[34] Ali A, Yousif M, Numan M, Kazmi AA. Coordinated generation and transmission expansion planning with energy storage systems to facilitate high penetration of renewable energy. IEEE Access 2025;13:176801–12. https://doi.org/10.1109/ACCESS.2025.3617374.
[35] Qiao L, Tan Q, Wen X, Wang Z. Complementary scheduling of hydro-wind-PV-storage systems: addressing flexibility demand for high-penetration variable renewable energy integration. Renew Energy 2026;257:124718. https://doi.org/10.1016/j.renene.2025.124718.
[36] Del Rosso AD, Eckroad SW. Energy storage for relief of transmission congestion. IEEE Trans Smart Grid 2014;5(2):1138–46. https://doi.org/10.1109/TSG.2013.2277411.
[37] Yan X, Gu C, Zhang X, Li F. Robust optimization-based energy storage operation for system congestion management. IEEE Syst J 2020;14(02):2694–702. https://doi.org/10.1109/JSYST.2019.2932897.
[38] Karimi A, Aminifar F, Fereidunian A, Lesani H. Energy storage allocation in wind integrated distribution networks: an MILP-Based approach. Renew Energy 2019;134:1042–55. https://doi.org/10.1016/j.renene.2018.11.034.
[39] Yuan W, Xin W, Su C, Cheng C, Yan D, Wu Z. Cross-regional integrated transmission of wind power and pumped-storage hydropower considering the peak shaving demands of multiple power grids. Renew Energy 2022;19:1112–26. https://doi.org/10.1016/j.renene.2021.10.046.
[40] Zhang X, Patelli E, Zhou Y, Chen D, Lian J, Xu B. Enhancing the economic efficiency of cross-regional renewable energy trading via optimizing pumped hydro storage capacity. Renew Energy 2025;240:0960–1481. https://doi.org/10.1016/j.renene.2024.122205.
[41] Lee D, Kim D, Joo S. Interval-stochastic programming for integrated generation, transmission, and Energy Storage System (ESS) planning considering uncertainty in renewable energy sources. IEEE Access 2025;13:30834–44. https://doi.org/10.1109/ACCESS.2025.3538649.
[42] Liao C, He L, Tan Z, Li Y, Chen C, Cao Y. Optimal planning method for scalable energy storage station in power system considering multiple application scenarios. Int J Electr Power Energy Syst 2025;172:111140. https://doi.org/10.1016/j.ijepes.2025.111140.
[43] Vargas LS, Bustos-Turu G, Larraín F. Wind power curtailment and energy storage in transmission congestion management considering power plants ramp rates. IEEE Trans Power Syst 2015;30(5):2498–506. https://doi.org/10.1109/TPWRS.2014.2362922.
[44] Zhao S, Suo X, Ma Y, Dong L. Multi-point layout planning for multi-energy power system based on complex adaptive system theory. CSEE J Power Energy Syst 2024;10(05):2138–46. https://doi.org/10.17775/CSEEJPES.2020.03550.
[45] Hossain M, Islam M, Muttaqi KM, Sutanto D, Agalgaonkar A. Component sizing and energy management for a supercapacitor and hydrogen storage based hybrid energy storage system to improve power dispatch scheduling of a wind energy system. IEEE Trans Ind Appl 2025;61(1):872–83. https://doi.org/10.1109/TIA.2024.3477417.
[46] Guo J, Chen J, Wu H, Zeng J, Peng J. Optimized scheduling and performance evaluation of hybrid energy storage systems with power-based and energy-based storage. Appl Energy 2025;395:126200. https://doi.org/10.1016/j.apenergy.2025.126200.
[47] Altea C, Yanagihara J. Optimizing pumped hydro and hydrogen storage for water-dependent renewable systems. Energy Nexus 2026;21:100634. https://doi.org/10.1016/j.nexus.2026.100634.
[48] Xu X, Wang K, Ma W, Wu C, Huang X, Ma Z, et al. Multi-objective particle swarm optimization algorithm based on multi-strategy improvement for hybrid energy storage optimization configuration. Renew Energy 2024;223:120086. https://doi.org/10.1016/j.renene.2024.120086.
[49] Yuan Q, Ma Q, Li B, Wang Z, Zhou X, Zhang Q, et al. Transfer capacity evaluation method of cross-regional channel based on tie-line feasible region analysis. Electr Power Autom Equip 2024;44(09):170–8. https://doi.org/10.16081/j.epae.202312023.
[50] Giraud BN, Rajaei A, Cremer JL. Constraint-driven deep learning for N-k security constrained optimal power flow. Electr Pow Syst Res 2024;235:110692. https://doi.org/10.1016/j.epsr.2024.110692.
[51] Li J, Liu X, Zheng Z, Xiao X, Zhang S, Gao H. Optimal planning and operation of multi-type flexible resources based on differentiated feature matching in regional power grid with high proportion of clean energy. J Mod Power Syst Clean Energy 2024;12(06):1724–36. https://doi.org/10.35833/MPCE.2023.000741.